

UCSF

UC San Francisco Previously Published Works

Title

NEMO reshapes the  $\alpha$ -Synuclein aggregate interface and acts as an autophagy adapter by co-condensation with p62.

Permalink

<https://escholarship.org/uc/item/14x6349k>

Journal

Nature Communications, 14(1)

Authors

Furthmann, Nikolas

Bader, Verian

Angersbach, Lena

et al.

Publication Date

2023-12-19

DOI

10.1038/s41467-023-44033-0

Peer reviewed

# NEMO reshapes the $\alpha$ -Synuclein aggregate interface and acts as an autophagy adapter by co-condensation with p62

---

Received: 8 February 2023

---

Accepted: 28 November 2023

---

Published online: 19 December 2023

---

 Check for updates

---

Nikolas Furthmann <sup>1</sup>, Verian Bader <sup>1,2</sup>, Lena Angersbach<sup>1</sup>, Alina Blusch<sup>3</sup>, Simran Goel<sup>1</sup>, Ana Sánchez-Vicente<sup>1</sup>, Laura J. Krause <sup>1,4</sup>, Sarah A. Chaban <sup>1</sup>, Prerna Grover <sup>2</sup>, Victoria A. Trinkaus<sup>5</sup>, Eva M. van Well<sup>1</sup>, Maximilian Jaugstetter<sup>6</sup>, Kristina Tschulik <sup>4,6</sup>, Rune Busk Damgaard <sup>7</sup>, Carsten Saft<sup>3</sup>, Gisa Ellrichmann<sup>3,20</sup>, Ralf Gold<sup>3</sup>, Arend Koch<sup>8</sup>, Benjamin Englert <sup>8,21</sup>, Ana Westenberger<sup>9</sup>, Christine Klein<sup>9</sup>, Lisa Jungbluth <sup>10,11</sup>, Carsten Sachse <sup>10,11,12</sup>, Christian Behrends <sup>13</sup>, Markus Glatzel <sup>14</sup>, F. Ulrich Hartl <sup>5,15</sup>, Ken Nakamura<sup>16,17</sup>, Chadwick W. Christine <sup>17,18</sup>, Eric J. Huang <sup>17,19</sup>, Jörg Tatzelt<sup>2,4</sup> & Konstanze F. Winklhofer <sup>1,4</sup> 


NEMO is a ubiquitin-binding protein which regulates canonical NF- $\kappa$ B pathway activation in innate immune signaling, cell death regulation and host-pathogen interactions. Here we identify an NF- $\kappa$ B-independent function of NEMO in proteostasis regulation by promoting autophagosomal clearance of protein aggregates. NEMO-deficient cells accumulate misfolded proteins upon proteotoxic stress and are vulnerable to proteostasis challenges. Moreover, a patient with a mutation in the NEMO-encoding *IKBKG* gene resulting in defective binding of NEMO to linear ubiquitin chains, developed a widespread mixed brain proteinopathy, including  $\alpha$ -synuclein, tau and TDP-43 pathology. NEMO amplifies linear ubiquitylation at  $\alpha$ -synuclein aggregates and promotes the local concentration of p62 into foci. In vitro, NEMO lowers the threshold concentrations required for ubiquitin-dependent phase transition of p62. In summary, NEMO reshapes the aggregate surface for efficient autophagosomal clearance by providing a mobile phase at the aggregate interphase favoring co-condensation with p62.

Cellular proteostasis is maintained by an elaborate network of protein quality control components, such as molecular chaperones, the ubiquitylation machinery, the proteasome, and the autophagy-lysosome pathway, to coordinate the proper triage, subcellular quarantine, and refolding or disposal of damaged proteins. In aging, proteotoxic stress along with a decline in the fidelity of protein quality control favors the accumulation of misfolded proteins, challenging the integrity of the cellular proteome. This is particularly relevant to postmitotic cells, such as neurons. In fact, the age-dependent accumulation of misfolded proteins is a characteristic feature of neurodegenerative diseases. Cells

are equipped with two proteolytic machineries, the ubiquitin-proteasome system and the autophagy-lysosomal system that remove misfolded proteins depending on their subcellular localization, their structure, oligomerization state and posttranslational modifications. Both degradation pathways are critically regulated by ubiquitin in cooperation with specific ubiquitin-binding proteins that target cargo to the proteasome or to selective autophagy<sup>1-6</sup>.

The selective autophagic degradation of aggregated proteins, referred to as aggrephagy, is mediated by several cargo receptors, such as p62/SQSTM1, NBR1, and TAX1BP1<sup>7-11</sup>. p62 and NBR1 both bind

---

A full list of affiliations appears at the end of the paper.  e-mail: [konstanze.winklhofer@rub.de](mailto:konstanze.winklhofer@rub.de)

to ubiquitinated cargo by their UBA (ubiquitin-associated) domains and cooperate as hetero-oligomers in forming local clusters on the cargo<sup>12–16</sup>. NBR1 recruits TAXBP1, which drives autophagosome biogenesis by interacting with FIP200, a scaffold protein of the core autophagy machinery<sup>16–18</sup>. Tethering of the aggregated cargo to the growing autophagosomal membrane is mediated by LC3 proteins, which bind to LIR (LC3-interacting region) motifs present in p62, NBR1, and TAXBP1. Finally, the cargo is engulfed by a double membrane and degraded upon fusion of the autophagosome with lysosomes.

Ubiquitylation is a multifaceted posttranslational modification, regulating a plethora of cellular processes. Its complexity is based on different variables, such as the number of ubiquitin molecules attached to substrates, the mode of inter-ubiquitin linkage, the formation of homo- and heterotypic chains, and the posttranslational modification of ubiquitin itself, for example by phosphorylation, SUMOylation, or NEDDylation<sup>19–22</sup>. In conventional ubiquitylation, the C-terminal glycine of ubiquitin is linked to one of seven lysine residues of another ubiquitin molecule by an isopeptide bond. Alternatively, the C-terminal glycine can be linked to the N-terminal methionine of the acceptor ubiquitin, resulting in the formation of a peptide bond<sup>23</sup>. This type of head-to-tail linkage is called linear or MI-linked ubiquitylation. Linear ubiquitin chains are exclusively generated by the RING-in-between-RING (RBR) E3 ubiquitin ligase HOIP, the catalytic component of the linear ubiquitin chain assembly complex (LUBAC). Within this complex, HOIP interacts with HOIL-1 and SHARPIN, which bind to the UBA domain of HOIP by their ubiquitin-like (UBL) domains, thereby activating autoinhibited HOIP<sup>24–33</sup>. LUBAC has mostly been studied in the context of immune signaling, NF- $\kappa$ B activation, and cell death regulation<sup>34–38</sup>. In these paradigms, the regulatory component of the IKK (inhibitor of  $\kappa$ B kinase) complex NEMO (nuclear factor- $\kappa$ B essential modulator), also called IKK $\gamma$ , is an important player, serving both as an interactor of linear ubiquitin chains and a substrate of HOIP<sup>39–41</sup>. Binding of NEMO to MI-linked ubiquitin chains via its UBAN (ubiquitin-binding in ABIN and NEMO) domain and also ubiquitylation of NEMO upon activation of innate immune receptors, such as the TNF receptor 1, induces a conformational change in NEMO and activates the associated kinases IKK $\alpha$  and IKK $\beta$ <sup>26,42,43</sup>. The activated IKK kinases phosphorylate I $\kappa$ B $\alpha$  (inhibitor of  $\kappa$ B $\alpha$ ), which is then modified by K48-linked ubiquitin chains and degraded by the proteasome. Thereby, NF- $\kappa$ B heterodimers, typically p65 and p50, are liberated from their binding to I $\kappa$ B $\alpha$  and translocate to the nucleus to regulate the expression of NF- $\kappa$ B-dependent genes.

Amorphic or hypomorphic mutations in the NEMO-encoding *IKBKG* gene located on the X-chromosome are associated with *Incontinentia pigmenti* (IP), a condition that is usually lethal in male fetuses and thus almost exclusively occurs in female patients with mosaic X-chromosome inactivation<sup>44–46</sup>. IP is a rare multisystem disorder that primarily affects the skin, but can also involve other ectodermal tissues including teeth, hair, nails, eyes, and the central nervous system<sup>47</sup>. IP-linked mutations comprise rearrangements, nonsense, frameshift, splice site, or missense variants<sup>45,46</sup>. Although IP can be inherited in an X-linked dominant fashion, between 65 and 75% of cases occur sporadically due to *de novo* mutations<sup>48</sup>. The phenotypic heterogeneity of the clinical presentation is based on the fact that throughout the body, cells expressing the wildtype *IKBKG* allele co-exist with cells expressing the mutant *IKBKG* allele, hampering the analysis of patients' bio-samples and the establishment of patient-derived cellular models. We identified a patient with IP who developed early onset, rapidly progressive neurodegeneration with a widespread mixed proteinopathy, including  $\alpha$ -synuclein, tau, and TDP-43 aggregates. The pathogenic p.Q330\* NEMO variant is compromised in NF- $\kappa$ B pathway activation, explaining the manifestation of IP, but in addition causes defective protein quality control. NEMO deficiency favors the accumulation of misfolded proteins and impairs the clearance of protein aggregates by autophagy. In this work, we reveal a critical function of NEMO in

proteostasis regulation by remodeling the aggregate interface and facilitating condensate formation of the autophagy cargo receptor p62.

## Results

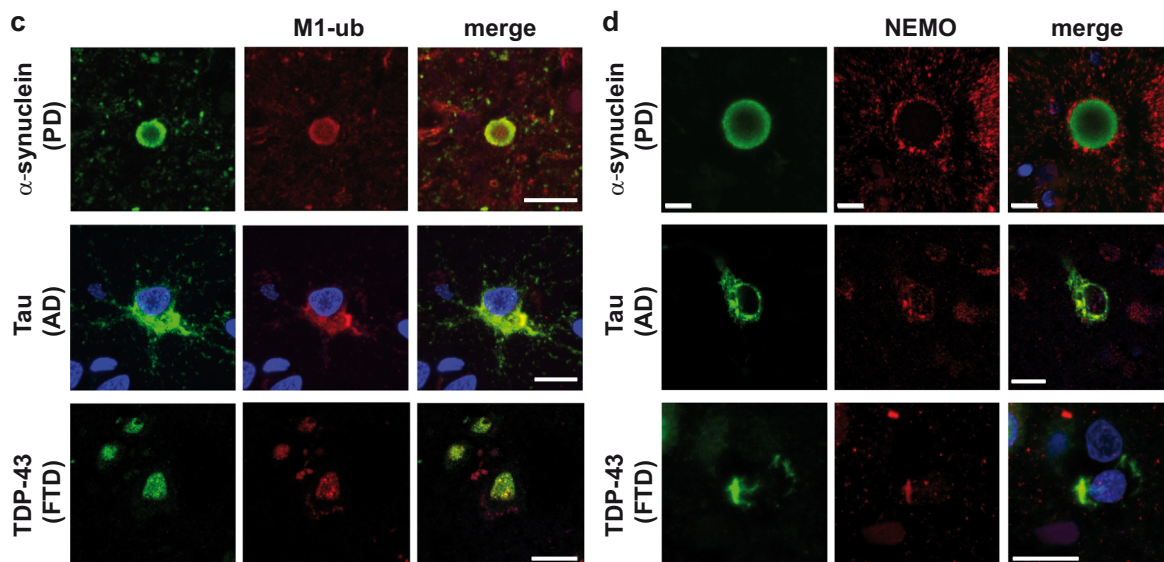
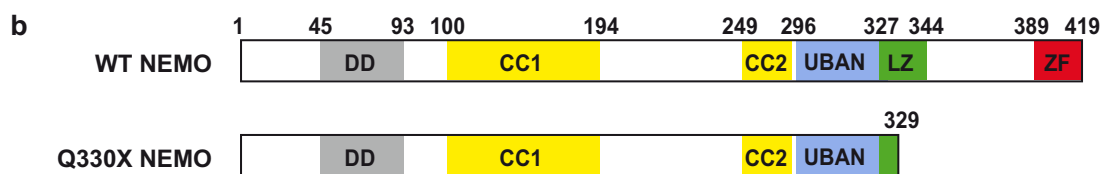
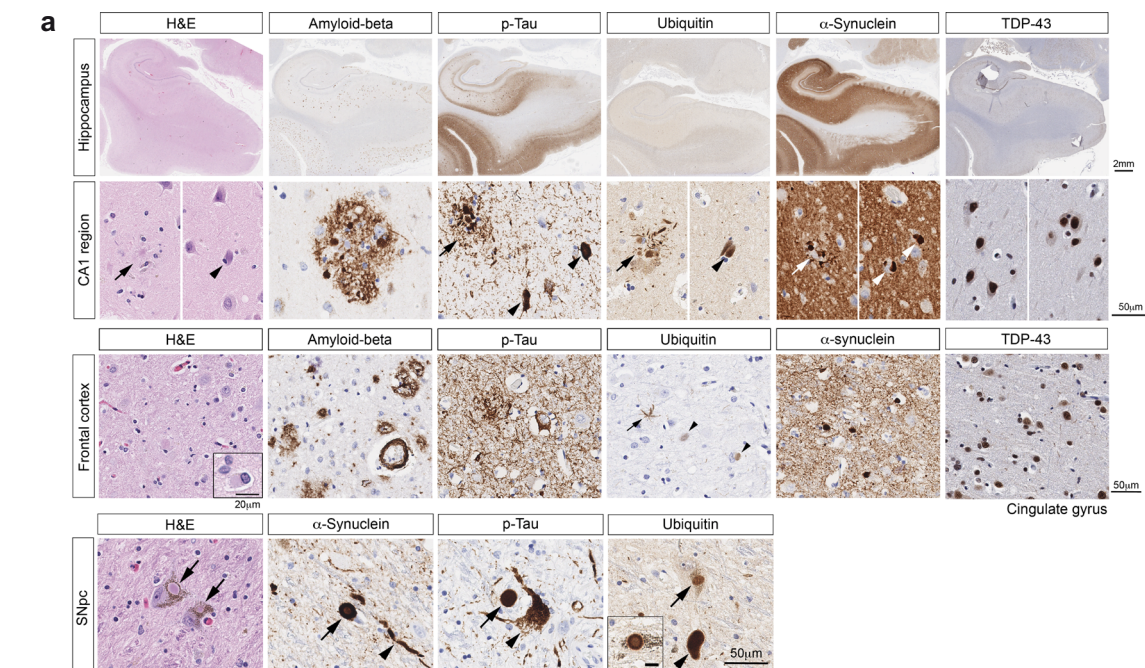
### A pathogenic variant in the *IKBKG* gene encoding NEMO is associated with a widespread mixed proteinopathy and progressive neurodegeneration

A female patient, who was diagnosed with IP during her infancy developed parkinsonism (left-sided bradykinesia, hypophonia, slowed gait) at age 48 years. She noted initial benefit with treatment with carbidopa/levodopa, but her condition rapidly progressed, forcing her retirement from work as a school teacher at age 52 years. A dopamine transporter scan was markedly abnormal, showing near absence of tracer uptake within the caudate and putamen bilaterally. She then developed severe cognitive impairment and died at age 56 years from progressive neurodegeneration. Brain autopsy revealed a widespread mixed proteinopathy, including  $\alpha$ -synuclein, tau, and TDP-43 aggregates with predominant  $\alpha$ -synuclein pathology (Fig. 1a). There was no family history of neurodegenerative diseases and whole-genome sequencing did not identify pathogenic or likely pathogenic variants in genes associated with neurodegenerative disorders (Supplementary Fig. 1). Genetic testing revealed a mosaic c.988 C > T nonsense mutation in the *IKBKG* gene, replacing glutamine at position 330 by a premature stop codon (p.Gln330\*). If translated, the resulting p.Q330\* NEMO variant would be truncated and lack the C-terminal region encompassing the leucine zipper (LZ) and zinc finger (ZF) (Fig. 1b).

Based on our previous finding that NEMO is recruited to misfolded huntingtin with a polyglutamine expansion (Htt-polyQ)<sup>49</sup>, we investigated whether an *IKBKG* gene mutation resulting in NEMO dysfunction is causally linked to neuronal protein aggregation observed in our patient. A functional characterization of NEMO p.Q330\* (hereafter referred to as Q330X) in cellular models showed that this mutant is defective in NF- $\kappa$ B signaling, explaining the clinical presentation with IP. In contrast to wildtype (WT) NEMO, Q330X NEMO was not able to promote TNF-induced degradation of I $\kappa$ B $\alpha$  or NF- $\kappa$ B transcriptional activity (Supplementary Fig. 2a–d). We observed impaired NF- $\kappa$ B activation by Q330X NEMO also upon IL-1 $\beta$  receptor activation<sup>50</sup>. However, our previous study revealed that HOIP was able to decrease Htt-polyQ aggregates independently of NF- $\kappa$ B activation<sup>49</sup>. Therefore, we studied whether NEMO is a downstream effector of LUBAC-mediated protein quality control. First, we tested if endogenous NEMO is recruited to protein aggregates other than Htt-polyQ. Indeed, immunohistochemistry of brain slices from patients with Parkinson's disease (PD), Alzheimer's disease (AD) or frontotemporal dementia (FTD) provided evidence for both NEMO and MI-linked ubiquitin chains co-localizing at aggregates formed by  $\alpha$ -synuclein, tau, or TDP-43 (Fig. 1c, d).

### NEMO deficiency promotes protein aggregation under proteotoxic stress

To analyze a possible role of NEMO in proteostasis regulation, we quantified the amount of protein aggregates induced by heat stress, proteasomal and lysosomal inhibition in wildtype and NEMO knockout (KO) embryonic fibroblasts (MEFs) by Proteostat<sup>®</sup>, a red fluorescent molecular rotor dye that binds to the cross-beta spine quaternary structure of aggregated proteins. In the absence of NEMO, protein aggregation was significantly increased in response to both heat stress and lysosomal inhibition, and a trend towards more aggregates was observed upon proteasomal inhibition (Fig. 2a, b). In addition, NEMO-deficient cells were more vulnerable to proteotoxic stress. Cell viability of NEMO KO MEFs was significantly decreased in response to heat stress, proteasomal or lysosomal inhibition compared to wildtype NEMO MEFs (Supplementary Fig. 3a–c). We then made use of a luciferase-based sensor of proteostasis capacity, the conformationally



destabilized double mutant firefly luciferase FlucDM (R188Q, R261Q) fused to EGFP<sup>51,52</sup>. Imbalances in proteostasis induce misfolding and aggregation of this sensor, which can be monitored by the formation of FlucDM-EGFP-positive foci and a decrease in its luciferase activity. With the help of this sensor we compared the effects of wildtype and Q330X NEMO under basal and proteotoxic stress conditions in a NEMO-deficient background. NEMO KO MEFs transiently expressing

FlucDM-EGFP and either wildtype or Q330X NEMO were quantified for the abundance of EGFP-positive foci and for luciferase activity. Heat stress (43 °C, 20 min) increased FlucDM-EGFP foci formation and decreased its luciferase activity in NEMO KO MEFs (Fig. 2c, d). Expression of wildtype NEMO significantly reduced foci formation and increased luciferase activity of FlucDM-EGFP under both basal and heat stress conditions, whereas Q330X NEMO had no effect (Fig. 2c, d).

**Fig. 1 | NEMO is associated with pathological protein aggregates.** **a** Widespread mixed brain proteinopathy in a patient expressing mutant Q330X NEMO. Both low and high magnification images show the presence of aggregated proteins, such as  $\alpha$ -synuclein, hyperphosphorylated tau, TDP-43, and amyloid beta in different brain regions. Many structures resembling Lewy body and Lewy neurites in pigmented neurons in the substantia nigra pars compacta (SNpc) are positive in immunostaining for  $\alpha$ -synuclein, hyperphosphorylated tau, and ubiquitin. Scale bars, as indicated. **b** Domain structure of wildtype (WT) human NEMO and mutant Q330X

NEMO. DD dimerization domain, CC1 coiled-coil 1 domain, CC2 coiled-coil 2 domain, UBAN ubiquitin-binding in ABIN and NEMO, LZ leucine zipper, ZF zinc finger. **c, d** MI-linked ubiquitin and NEMO co-localize with  $\alpha$ -synuclein, tau, and TDP-43 aggregates in human brain. Immunofluorescent stainings of cortical or midbrain sections from patients with Parkinson's disease (PD), Alzheimer's disease (AD), or frontotemporal dementia (FTD). Brain sections were stained with antibodies against MI-ubiquitin (**c**), NEMO (**d**), and  $\alpha$ -synuclein (PD), tau (AD), or TDP-43 (FTD); DAPI (blue). Scale bar, 10  $\mu$ m.

Interestingly, NF- $\kappa$ B was not activated by heat stress, as shown by an NF- $\kappa$ B luciferase reporter assay and a p65 nuclear translocation assay (Fig. 2e, f). In conclusion, NEMO plays a role in proteostasis regulation that seems to be independent of NF- $\kappa$ B activation.

### Misfolded $\alpha$ -synuclein is decorated with MI-linked ubiquitin and NEMO

Since the NEMO mutant patient showed a predominant  $\alpha$ -synuclein pathology, we employed cellular models of  $\alpha$ -synuclein (aSyn) aggregation for mechanistic studies. Recombinant A53T aSyn preformed fibrils (PFFs) were added as seeds to SH-SY5Y cells stably expressing A53T aSyn fused to GFP (aSyn-GFP) to induce aggregation of aSyn-GFP<sup>53–55</sup>. Intracellular aSyn aggregates formed upon seeding showed characteristic features of pathologic aSyn, such as phosphorylation at serine 129 and insolubility in detergents, as determined by immunocytochemistry and immunoblotting, respectively (Supplementary Fig. 4a, b). In addition, we characterized the aSyn seeds by Thioflavin T fluorescence, dynamic light scattering, and liquid atomic force microscopy (Supplementary Fig. 5a–f).

Consistent with our observation that MI-linked ubiquitin occurs at Lewy bodies in human brain (Fig. 1c), linear ubiquitin chains colocalized with aSyn aggregates in SH-SY5Y cells after seeding (Fig. 3a). Moreover, seeding of primary cortical neurons induced misfolding and serine 129 phosphorylation of endogenous aSyn, which stained positive for MI-linked ubiquitin (Fig. 3b). The presence of linear ubiquitin chains at aSyn in seeded SH-SY5Y cells was confirmed biochemically by affinity purification of aSyn-GFP followed by immunoblotting using MI-ubiquitin-specific antibodies<sup>56</sup> (Fig. 3c). Moreover, endogenous NEMO was significantly enriched at seeded aSyn aggregates (Fig. 3d) and all three LUBAC components were recruited to aSyn aggregates (Fig. 3e). In contrast, the RBR E3 ubiquitin ligase ARIH1 (Ariadne homolog 1), used as a control, was not recruited to aSyn aggregates (Fig. 3e).

### The Q330X NEMO mutant does not bind to MI-linked ubiquitin chains and is not ubiquitylated by HOIP

To gain further insight into the function of NEMO in proteostasis regulation, we compared the effect of wildtype NEMO and Q330X NEMO on aSyn aggregates in the SH-SY5Y seeding model. We first tested for NEMO recruitment and observed that Q330X NEMO did not efficiently co-localize with aSyn aggregates, whereas wildtype NEMO was strongly enriched at aSyn aggregates (Fig. 4a). Defective recruitment of Q330X NEMO to protein aggregates was confirmed in SH-SY5Y cells with Htt-polyQ (Htt-Q97) aggregates, indicating that this phenomenon is not limited to aSyn aggregates (Fig. 4b). We also performed filter retardation assays using the SDS-insoluble fraction of Htt-Q97-expressing NEMO KO MEFs reconstituted with either wildtype, Q330X or K285R/K309R NEMO. The K285R/K309R NEMO mutant lacks two critical lysine residues required for NEMO linear ubiquitylation<sup>57</sup>. In contrast to wildtype NEMO, Q330X or K285R/K309R NEMO were less efficiently retained by the membrane together with Htt-Q97, suggesting decreased abundance of these mutants at Htt-Q97 aggregates (Fig. 4c).

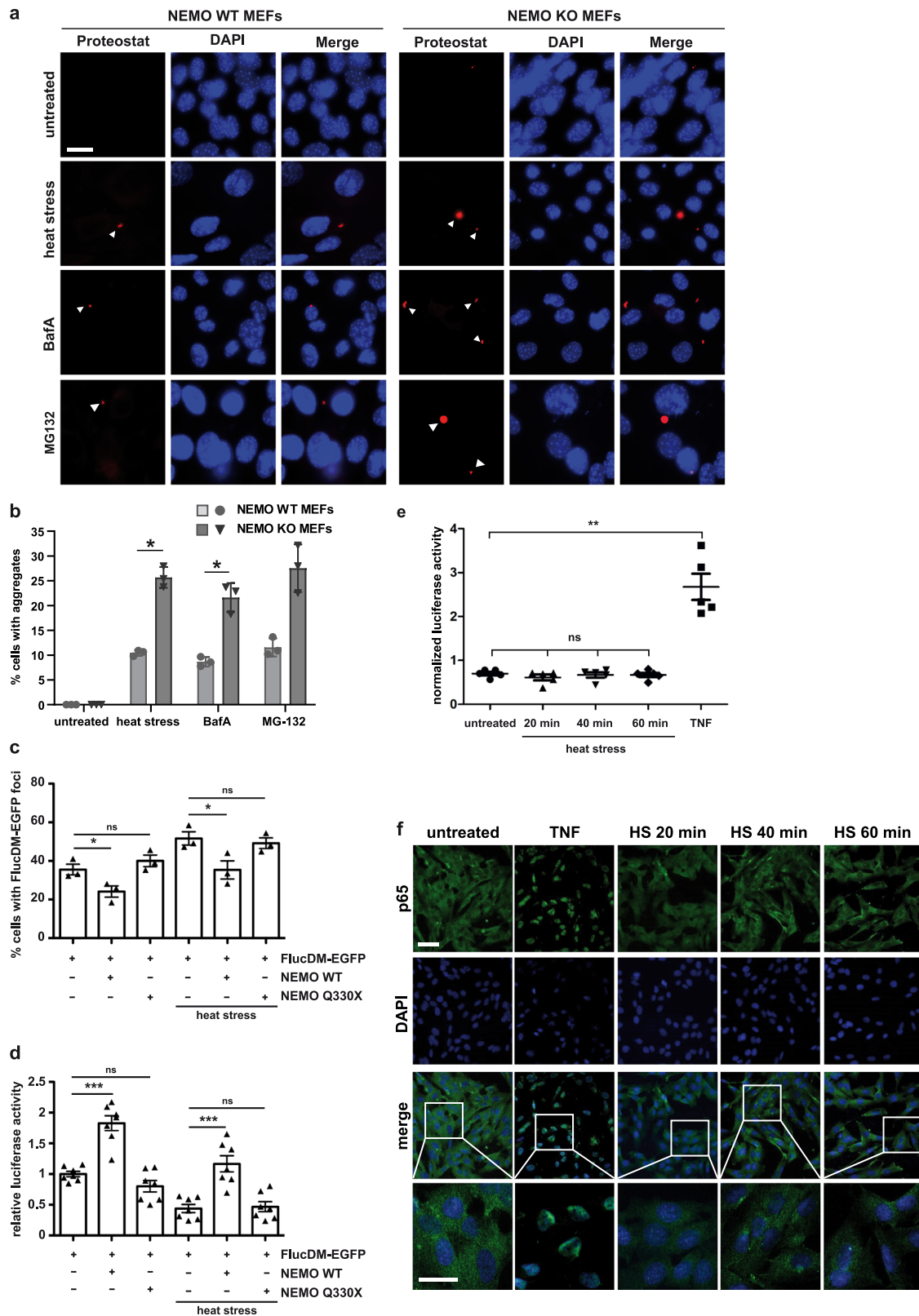
We previously found that NEMO is recruited to Htt-polyQ aggregates by binding to linear ubiquitin chains generated by HOIP<sup>49</sup>. Therefore, we compared the capacity of wildtype NEMO and Q330X

NEMO to bind linear ubiquitin chains. Lysates of cells expressing either wildtype or Q330X HA-tagged NEMO were incubated with recombinant tetra-MI-ubiquitin (4 $\times$ MI-ub), then NEMO was affinity-purified via its HA tag and immunoblotted using MI-ubiquitin-specific antibodies. In contrast to wildtype NEMO, Q330X NEMO did not bind to tetra-MI-ubiquitin, although the UBAN domain (residues 296–327) is not affected by the C-terminal deletion (Fig. 4d). Moreover, Q330X NEMO was not modified by linear ubiquitin chains, although the key ubiquitin acceptor lysine residues (K285 and K309) are present in this mutant<sup>57</sup>. We induced MI-ubiquitination of HA-tagged NEMO by either treating the cells with TNF or overexpressing the LUBAC components HOIP, HOIL-1L, and SHARPIN (Fig. 4e). The cells were lysed under denaturing conditions, NEMO was immunoprecipitated via its HA tag and analyzed by immunoblotting using MI-ubiquitin-specific antibodies. Whereas wildtype NEMO was MI-ubiquitylated in both conditions, Q330X NEMO was not even ubiquitylated upon the overexpression of LUBAC (Fig. 4e). Next, we analyzed the interaction of wildtype NEMO and Q330X NEMO with endogenous HOIP by co-immunoprecipitation experiments. The NZF1 domain of HOIP interacts with the coiled-coil 2 (CC2) region upstream the UBAN domain of NEMO<sup>57–59</sup>. HOIP did not co-purify with Q330X NEMO, which helps to explain why Q330X NEMO is not ubiquitylated (Fig. 4f).

Since NEMO not only binds to MI-linked polyubiquitin but also is covalently modified by HOIP, we followed up the hypothesis that NEMO increases MI-ubiquitylation at aSyn aggregates. We generated NEMO KO SH-SY5Y cells by CRISPR/Cas9 and induced aggregation of transiently expressed aSyn-GFP by adding aSyn seeds. NEMO KO SH-SY5Y cells were reconstituted with either wildtype NEMO or Q330X NEMO and the colocalization of MI-linked ubiquitin, NEMO, and aSyn aggregates was quantified by the Pearson coefficient. Colocalization of MI-linked ubiquitin and aSyn was strongly reduced when Q330X NEMO was expressed in comparison to wildtype NEMO (Fig. 4g, h, Supplementary Fig. 6a), suggesting that NEMO amplifies MI-ubiquitylation at aSyn aggregates. A disadvantage of the aSyn seeding model regarding biochemical studies is the low aggregation efficiency due to the fact that PFFs are taken up only by a subfraction of cells. To add more evidence for the role of NEMO in increasing the abundance of MI-linked ubiquitin at aggregates, we therefore used cells expressing Htt-Q97, resulting in aggregate formation in all cells transfected with Htt-Q97. HEK293T cells expressing Htt-Q97 or Htt-Q97 together with either wildtype NEMO, Q330X NEMO, or D311N NEMO, a mutant that is defective in binding to MI-linked ubiquitin<sup>60,61</sup>, were lysed 72 h after transfection under denaturing conditions. The SDS-insoluble pellets containing the Htt-Q97 aggregates were dissolved in formic acid and analyzed by immunoblotting. Wildtype NEMO but neither Q330X nor D311N NEMO increased the MI-linked ubiquitin-specific signal, supporting the MI-ubiquitin-amplifying function of NEMO at protein aggregates (Fig. 4i).

### A local NF- $\kappa$ B signaling platform is assembled at aSyn aggregates which does not promote a functional response

It has been shown recently that LUBAC is recruited to intracellular bacteria, such as *Salmonella enterica*, which can escape vacuoles and invade the cytosol<sup>62–64</sup>. Modification of the bacterial surface with linear ubiquitin chains by HOIP induces anti-bacterial autophagy (xenophagy) and recruits NEMO for local activation of NF- $\kappa$ B. We therefore



tested whether an NF- $\kappa$ B signaling platform is also assembled at aSyn aggregates. Indeed, endogenous phospho-IKK $\alpha$ / $\beta$  (p-IKK $\alpha$ / $\beta$ ), p65, and phospho-p65 (p-p65) were strongly enriched at aSyn aggregates (Fig. 5a). However, we did not observe nuclear translocation of the NF- $\kappa$ B subunit p65 on day 1, 2, or 3 after seeding (Fig. 5b, c). To test whether NF- $\kappa$ B signaling is compromised in the presence of aSyn aggregates, we treated aSyn-expressing cells with TNF on day 1, 2 and 3

after seeding. Whereas almost 100% of non-seeded cells showed nuclear translocation of p65 in response to TNF treatment, p65 translocation was significantly reduced upon seeding with only about 50% of cells positive for nuclear p65 on day 3 after seeding (Fig. 5b, c). Super-resolution structured illumination fluorescence microscopy (SR-SIM) revealed that p65 is trapped at aSyn aggregates upon TNF stimulation, whereas in cells without aSyn aggregates, TNF-induced

**Fig. 2 | NEMO protects from proteotoxic stress. a b** NEMO-deficient cells are prone to protein aggregation under proteotoxic stress. **a** NEMO wildtype (WT) and knockout (KO) embryonic fibroblasts (MEFs) were heat stressed (42 °C, 1 h) or treated with the proteasomal inhibitor MG-132 (0.5 μM, 48 h) or the lysosomal inhibitor Bafilomycin A1 (BafA, 100 nM, 48 h) and then stained by Proteostat® to detect protein aggregates. Scale bar: 20 μm. **b** Cells positive for aggregates were quantified. All data are displayed as mean ± SD based on 3 independent experiments, analyzed by two-way ANOVA followed by Šidák's multiple comparisons test. At least 150 cells were assessed per condition. Heat stress: \**p* = 0.0283, BafA: \**p* = 0.0414. **c, d** Wildtype NEMO but not Q330X NEMO decreases misfolding of the folding sensor FlucDM-EGFP-luciferase. NEMO KO MEFs transiently expressing FlucDM-EGFP-luciferase and either wildtype (WT) NEMO or Q330X NEMO were subjected to a heat stress (HS, 43 °C, 20 min) 48 h after transfection or left untreated. **c** The cells were then analyzed by immunocytochemistry and fluorescence microscopy. Shown is the fraction of NEMO-expressing cells with EGFP-

positive foci. Data represent mean ± SEM based on 3 independent experiments. At least 900 transfected cells have been analyzed per condition. Statistics: one-tailed Mann–Whitney *U*-tests \**p* ≤ 0.05. **d** In parallel, luciferase activity of control and heat stressed cells were analyzed luminometrically. Data represent mean ± SEM based on 7 independent experiments. Statistics: One-way ANOVA with Bonferroni's multiple comparison posthoc test; \*\*\**p* ≤ 0.001. **e, f** Transient heat stress does not activate NF-κB signaling. **e** HEK293T cells transiently expressing an NF-κB-luciferase reporter construct were heat stressed for 20, 40, or 60 min (42 °C) and 8 h later luciferase activity was quantified. As a positive control, one set of cells was treated with TNF (10 ng/ml, 8 h). Data are shown as normalized mean ± SD based on 5 independent biological replicates. \*\**p* ≤ 0.01. **f** SH-SY5Y cells were heat stressed (42 °C) for the indicated time and then nuclear translocation of the NF-κB subunit p65 was analyzed by immunocytochemistry and fluorescence microscopy using antibodies against p65. As a positive control, one set of cells was treated with TNF (25 ng/ml, 15 min). Scale bar, 10 μm (overview) and 10 μm (inset).

efficient nuclear translocation of p65 (Fig. 5c). Moreover, TNF-induced nuclear translocation was also impaired in SH-SY5Y cells expressing Htt-Q97, suggesting that pathogenic protein aggregates interfere with NF-κB signaling (Fig. 5d). These results indicated that although NF-κB is locally activated at aggregates, functional NF-κB signaling is impaired most probably through sequestration of p65 and possibly other NF-κB pathway components at the aggregates.

### NEMO promotes autophagosomal degradation of α-synuclein in a p62-dependent manner

Our previous data indicated that NEMO is recruited to aSyn aggregates along with other NF-κB signaling components without inducing a functional NF-κB response. Thus, NEMO seems to have an NF-κB-independent role in proteostasis regulation. Along this line, different protein aggregates accumulated in the brain of the Q330X NEMO patient, and wildtype NEMO but not Q330X NEMO reduced the fraction of cells with FlucDM-EGFP aggregates. LUBAC promotes the autophagic clearance of cytosol-invading bacteria<sup>62–64</sup>, we therefore wondered whether linear ubiquitin chains can influence the degradation of protein aggregates by autophagy.

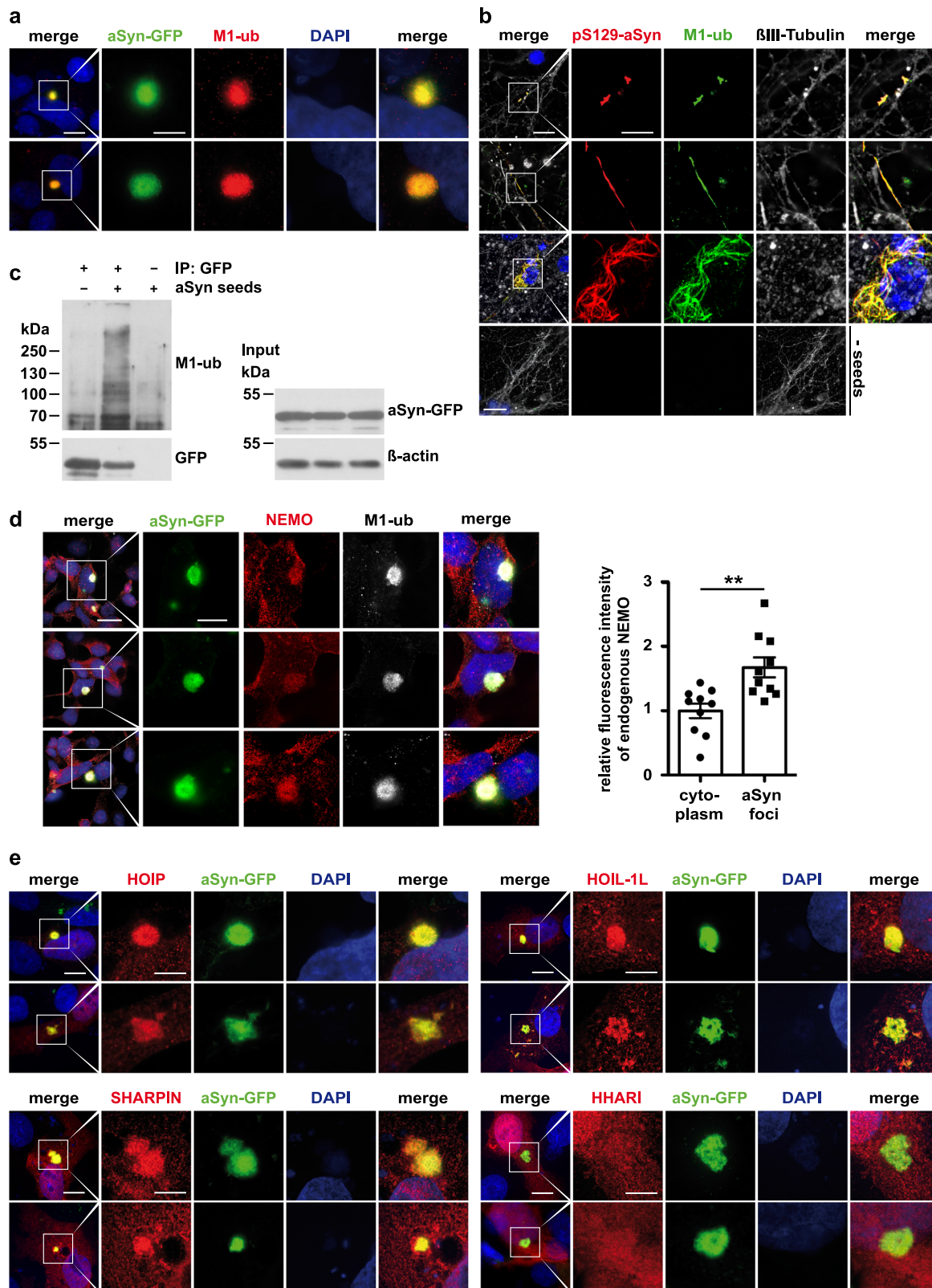
Intracellular aSyn can be degraded by both the proteasome and lysosomes depending on its posttranslational modifications, conformational state, and subcellular localization<sup>65–67</sup>. To test whether linear ubiquitylation promotes degradation of aSyn aggregates via autophagy, we transiently expressed NEMO or HOIP in SH-SY5Y cells and quantified the fraction of cells with aSyn aggregates 48 h after seeding. Both wildtype NEMO and wildtype HOIP, but neither Q330X NEMO nor catalytically inactive C885A HOIP, decreased the number of cells with aSyn aggregates (Fig. 6a, b). Notably, inhibition of lysosomal degradation by bafilomycin A1 abolished the ability of NEMO and HOIP to reduce the number of cells with aSyn aggregates (Fig. 6a, b). We also tested the D311N NEMO mutant, compromised in binding to M1-linked ubiquitin<sup>60,61</sup>. Similarly to Q330X NEMO, M1- and K63-ubiquitylation of D311N NEMO was impaired (Supplementary Fig. 6b). Also, it was not recruited to aSyn aggregates (Supplementary Fig. 6c) and did not reduce aSyn aggregates (Fig. 6a). To validate our observations for endogenous NEMO and HOIP, we downregulated the expression of NEMO or HOIP by RNA interference in the aSyn seeding model. Silencing of NEMO or HOIP increased the number of cells with aSyn aggregates to a similar extent (Fig. 6c), corroborating our results with NEMO or HOIP overexpression.

Since NEMO and HOIP apparently promote the degradation of misfolded aSyn depending on lysosomal function, we aimed at uncovering the underlying mechanism. Ubiquitylation is decoded and translated into cellular effects by specific ubiquitin-binding proteins. We reasoned that p62/SQSTM1 might be a promising candidate to test in our paradigm, based on its key role in targeting protein aggregates for selective autophagy<sup>5,12,68–70</sup>. The ubiquitin-binding UBA domain of p62, which is required to shuttle cargo to the autophagic machinery,

binds to M1-linked ubiquitin with the strongest affinity compared to other ubiquitin linkages<sup>71</sup>. Moreover, p62 has been reported to interact with NEMO<sup>72–74</sup> and to co-localize with Lewy bodies<sup>75,76</sup>. We confirmed that endogenous p62 binds to aSyn aggregates in our seeding model (Fig. 6d) and that the recruitment of p62 to aSyn aggregates depends on its UBA domain (Supplementary Fig. 6d). Co-immunoprecipitation experiments using cell lysates revealed that in contrast to wildtype NEMO, the Q330X NEMO mutant does not interact with endogenous p62 (Fig. 6e).

To test for a role of p62 in mediating effects downstream of linear ubiquitylation, we analyzed aSyn aggregates in p62-deficient MEFs (p62 KO MEFs) expressing aSyn-GFP. Two days after seeding, about 75% of aSyn-GFP-expressing p62 KO MEFs displayed aSyn aggregates. Restoring p62 expression in p62 KO MEFs decreased the fraction of aggregate-positive cells to about 55%, similarly to the extent of aSyn aggregation observed in wildtype SH-SY5Y cells. Notably, the rescue effect of p62 was dependent on its UBA domain, since expression of p62-ΔUBA had no effect on the number of cells with aSyn aggregates in p62 KO MEFs (Fig. 6f). Increased expression of NEMO or HOIP in p62-deficient cells revealed a p62-dependent effect of both NEMO and HOIP, seen after reconstituting p62 KO MEFs with wildtype p62 in comparison to p62-ΔUBA (Fig. 6f). In addition, we observed a minor p62-independent effect in reducing aSyn aggregates, most probably mediated by other ubiquitin-binding autophagy receptors. Notably, the p62-dependent effect of NEMO was blocked by bafilomycin A1, confirming that p62 decreased aSyn aggregates downstream of NEMO by autophagosomal clearance (Fig. 6g).

Next, we wondered whether defective p62-dependent autophagosomal degradation of aSyn might explain the accumulation of aSyn aggregates in the Q330X NEMO patient. We analyzed brain sections from the Q330X NEMO patient by immunohistochemistry and found that colocalization of p62 with aSyn-positive aggregates was significantly reduced in comparison to patients suffering from other α-synucleinopathies, such as Dementia with Lewy Bodies (DLB) (Fig. 7a, b). Of note, p62 signal intensity was strongly increased in the Q330X NEMO patient's brain, possibly reflecting a compensatory upregulation of p62 expression (Fig. 7c). Encouraged by these findings, we wondered whether an influence of NEMO on p62 recruitment to aSyn aggregates is also evident in cellular models. We induced aggregation of transiently expressed aSyn-GFP in wildtype and NEMO KO SH-SY5Y cells by adding aSyn seeds and visualized endogenous p62 by SR-SIM, which revealed a striking difference in the pattern of p62 localization at the aggregates. Whereas p62 mostly formed foci at the aggregate surface in the presence of NEMO, it showed a more diffuse distribution around the aggregates in the absence of NEMO (Fig. 7d). The same NEMO-dependent differences in the localization pattern at aSyn aggregates were observed for the autophagy receptor NBR1 (Fig. 7e), which cooperates with p62 in forming local clusters on protein aggregates<sup>16</sup>. Ubiquitin-dependent p62 condensation is required for efficient



autophagic clearance of cargo<sup>14–16,77,78</sup>, we therefore tested whether the non-condensated localization of p62 and NBR1 at aggregates has consequences on subsequent steps of the autophagic process. Indeed, the abundance of both LC3 and LAMP2 at aSyn aggregates was significantly decreased in NEMO KO cells (Fig. 7f, g). Thus, in the absence of NEMO, p62 and NBR1 are impaired in clustering at aggregated cargo, which compromises recruitment of the autophagic machinery.

**NEMO promotes p62 condensate formation at aggregates by lowering the threshold for ubiquitin-induced phase transition**  
We and others recently observed that NEMO undergoes phase separation upon binding to linear ubiquitin chains<sup>50,79</sup>. Since Q330X NEMO is impaired in binding to M1-linked ubiquitin, it does neither phase-separate in vitro nor form condensates in cells<sup>50</sup>. We therefore speculated that NEMO by interacting with M1-linked ubiquitin chains



**Fig. 3 | NEMO and LUBAC components are recruited to aSyn aggregates.** **a** MI-linked ubiquitin is enriched at aSyn aggregates formed in the cellular aSyn seeding model. SH-SY5Y cells stably expressing aSyn A53T-GFP were treated with aSyn A53T seeds, fixed 72 h after seeding, and analyzed by immunocytochemistry and fluorescence SR-SIM using MI-ubiquitin-specific antibodies. Scale bar, 10  $\mu$ m (overview) and 5  $\mu$ m (inset). **b** MI-linked ubiquitin colocalizes with pS129-aSyn-positive neurites in primary neurons. Primary cortical neurons were treated with aSyn A53T seeds at day 5 in vitro to induce aggregation of endogenous aSyn, fixed 7 days (rows 1 and 2) or 10 days (rows 3 and 4) after seeding, and analyzed by immunocytochemistry and fluorescence SR-SIM using antibodies against pS129-aSyn, MI-linked ubiquitin, and  $\beta$ III-Tubulin. Scale bar, rows 1, 2, and 3: 10  $\mu$ m (overview) and 5  $\mu$ m (inset), row 4: 20  $\mu$ m. **c** MI-linked ubiquitin co-immunoprecipitates with aSyn. SH-SY5Y cells stably expressing A53T-GFP aSyn were treated with aSyn A53T seeds for 72 h, lysed in 1% Triton X-100 in PBS, and aSyn-GFP was immunoprecipitated using GFP-trap beads. An immunoprecipitation with anti-HA beads was used to control for nonspecific binding. The pellet was analyzed by immunoblotting for MI-

linked ubiquitin and GFP. The input was immunoblotted against aSyn and  $\beta$ -actin. **d** Endogenous NEMO is enriched at aSyn aggregates. SH-SY5Y cells stably expressing aSyn A53T-GFP were treated as described in a and analyzed by immunocytochemistry and fluorescence SR-SIM using antibodies against NEMO and MI-linked ubiquitin. Scale bar, 20  $\mu$ m (overview) and 10  $\mu$ m (inset). For quantification of the relative NEMO fluorescent signals, the NEMO-specific signal at aSyn-GFP aggregates was compared to a cytoplasmic area outside aSyn aggregates. The mean intensity within the cytoplasm was set to 1. Data represent mean  $\pm$  SEM ( $n = 10$ ). Statistics: Two-tailed  $t$ -test,  $^{**}p = 0.0026$ . **e** LUBAC components are recruited to aSyn aggregates. SH-SY5Y cells stably expressing  $\alpha$ -Synuclein A53T-GFP were transiently transfected with plasmids encoding either HA-HOIP, HA-HOIL-1L, or HA-SHARPIN, or HA-HHARI as a control. One day after transfection, the cells were treated with aSyn A53T seeds, fixed 48 h after seeding, and analyzed by immunocytochemistry and fluorescence SR-SIM using antibodies against the HA-tag. Scale bar, 10  $\mu$ m (overview) and 5  $\mu$ m (inset).

at protein aggregates may prime the aggregate surface for efficient p62 condensate formation. Fluorescence recovery after photobleaching (FRAP) of Halo-tagged NEMO expressed in NEMO KO cells indicated that NEMO forms a mobile phase at aSyn aggregates, whereas the aSyn aggregates show a non-dynamic behavior (Fig. 8a, b). We also observed by SR-SIM microscopy that endogenous p62, NEMO, and MI-linked ubiquitin co-localize in condensates at aSyn aggregates (Fig. 8c). Next, we tested a possible role of MI-linked ubiquitin in mediating the interaction between NEMO and p62 by using recombinantly expressed proteins. Wildtype or Q330X NEMO fused to MBP (maltose-binding protein) was mixed with mCherry-p62 in the presence or absence of MI-linked tetra-ubiquitin (4 $\times$ MI-ub). NEMO was immunoprecipitated by MBP-specific antibodies and immunoblotted for p62. In the absence of 4 $\times$ MI-ub, the p62 signal upon co-purification with NEMO was minimally increased over background, but strongly increased in the presence of 4 $\times$ MI-ub (Fig. 8d). Similarly to the co-immunoprecipitation experiments in cellular lysates, p62 did not co-purify with Q330X NEMO, confirming that defective binding of linear ubiquitin to Q330X NEMO also affects its interaction with p62 (Fig. 8d).

Our SR-SIM images indicated a foci-like staining also for NEMO and MI-linked ubiquitin at aggregates (Fig. 8c). This observation prompted us to study a possible effect of NEMO on ubiquitin-induced p62 condensation in vitro. We first tested whether p62 and NEMO can co-condensate. Recombinant mCherry-p62 and NEMO-GFP were mixed with or without recombinant tetra- or octa-MI-linked ubiquitin. Laser scanning microscopy revealed that co-condensation of p62 and NEMO occurred in presence of tetra- or octa-MI-linked ubiquitin, but not in the absence of MI-linked ubiquitin (Fig. 8e). We then studied p62 condensate formation dependent on the concentration of p62 and tetra- or octa-MI-linked ubiquitin (from 0.5 to 10  $\mu$ M each) in the presence and absence of NEMO. As illustrated by phase diagrams, NEMO shifted p62 phase transition to the lowest concentration of both p62 and tetra- or octa-MI-ubiquitin (Fig. 8f). Thus, by co-condensation with p62 and MI-linked ubiquitin, NEMO facilitates the local concentration of p62. These results provide a mechanistic explanation for the impaired autophagic clearance of protein aggregates in the absence of functional NEMO observed in our cellular models and the Q330X NEMO patient brain samples.

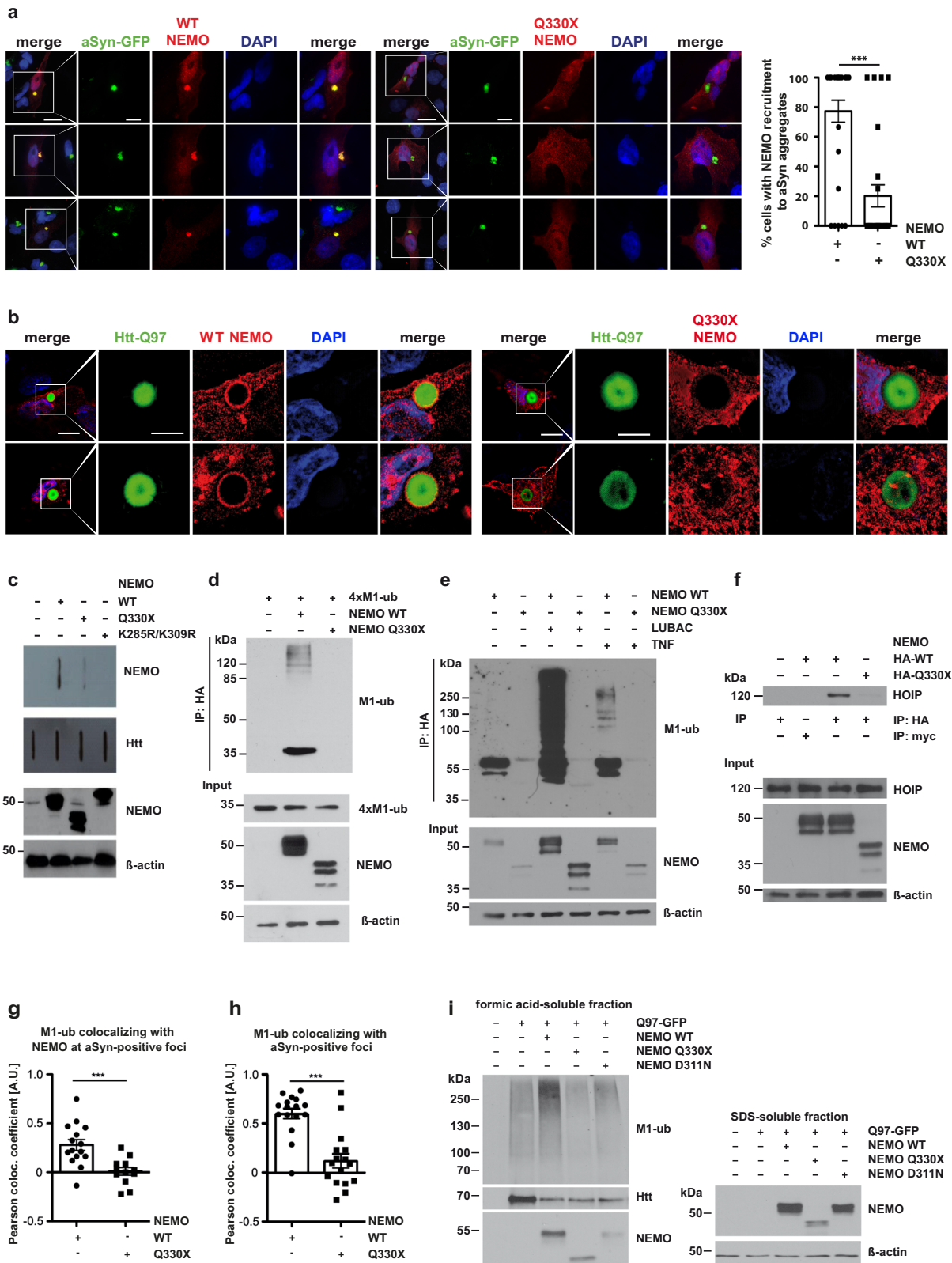
## Discussion

Here we demonstrate that NEMO has an NF- $\kappa$ B-independent role in maintaining cellular proteostasis by acting as an autophagy adapter protein. NEMO-deficient cells accumulate misfolded proteins upon proteotoxic stress and are hypersensitive to proteostasis dysregulation. The crucial role of NEMO in maintaining proteostasis was confirmed by the neuropathological alterations found in the Q330X NEMO mutant patient, who shows a progressive widespread mixed brain proteinopathy with predominant aSyn pathology. Studying this NEMO

variant revealed that LUBAC-mediated formation of linear ubiquitin chains and binding of NEMO to linear ubiquitin chains are required to promote autophagosomal degradation of misfolded aSyn through the selective autophagy receptor p62. We previously reported that wild-type NEMO in contrast to Q330X NEMO has the propensity to form phase-separated condensates upon binding to linear ubiquitin chains<sup>50</sup>. Here we show that through this propensity NEMO facilitates p62-dependent aggregate formation with ubiquitinated cargo is a crucial event in p62-mediated autophagy, since it contributes to the recruitment of the autophagic machinery<sup>14–16,77,78</sup>. Whereas the mechanism of autophagy initiation by p62 has been studied in great detail, little is known about processes at the aggregate interface required to locally concentrate and rearrange p62. Our study identified NEMO as a major player in priming the aggregate interphase for p62 condensation. At least two NEMO-dependent processes seem to be relevant in this context. First, NEMO amplifies linear ubiquitination at protein aggregates. This is accomplished by both binding to MI-linked ubiquitin via its UBAN domain and being MI-ubiquitylated by HOIP. HOIP is recruited to protein aggregates by VCP/p97 and can generate free, unanchored MI-linked polyubiquitin<sup>49</sup> or assemble MI-linked ubiquitin chains on pre-existing K63-linked chains<sup>80</sup>, suggesting that the aggregated protein not necessarily needs to be modified directly by HOIP. Moreover, NEMO is a HOIP substrate available at protein aggregates. Accordingly, we found MI-linked ubiquitin and NEMO at various protein aggregates, including aSyn, Htt-polyQ, tau, and TDP-43. Second, binding of NEMO to MI-linked ubiquitin generates a mobile phase-separated aggregate surface, facilitating the local concentration of p62 by co-condensation. Indeed, liquidity at the cargo surface seems to be an important prerequisite for efficient selective autophagy<sup>81–85</sup>.

The Q330X NEMO mutant lacks the C-terminal region including part of the LZ and the ZF domain. The region between the CC2 (coiled-coil 2) and LZ domain includes the UBAN domain and forms elongated parallel coiled-coil dimers<sup>59</sup>. This region is required for binding to polyubiquitin, dimerization and interaction with HOIP<sup>57–59</sup>. The UBAN domain binds MI-linked polyubiquitin chains 100-fold stronger compared to K63-linked chains, whereas the C-terminal ZF binds K63-linked polyubiquitin chains with high affinity<sup>61,86–90</sup>. The ZF has also been reported to mediate binding to I $\kappa$ B $\alpha$ <sup>91</sup> and to the ubiquitin chain-editing enzyme A20, a negative regulator of NF- $\kappa$ B activation<sup>92</sup>. Although the UBAN domain is present in the Q330X NEMO mutant, it cannot bind to MI-linked ubiquitin, most likely caused by conformational alterations or impaired dimer formation of Q330X NEMO.

The UBAN domain is an MI-ubiquitin-binding domain present in NEMO, Optineurin, and ABIN-1-3 (A20-binding inhibitors of NF- $\kappa$ B)<sup>87</sup>. Whereas these UBAN proteins show differences in their ubiquitin-binding properties and their biological functions<sup>93</sup>, they share a link to autophagy. Optineurin is a well-characterized autophagy receptor in



mitophagy, xenophagy and aggrephagy<sup>8,11</sup>, and ABIN-1 has recently been linked to mitophagy<sup>94</sup>. In contrast to Optineurin and ABIN-1, NEMO has no LIR domain to directly interact with LC3. It rather functions as an indirect autophagy adapter protein by interacting with p62 in an M1-ubiquitin-dependent manner. Interestingly, the *Drosophila melanogaster* NEMO homolog Kenny has a LIR motif that interacts with Atg8/LC3 and promotes the autophagic degradation of the IKK

complex in order to prevent constitutive production of antimicrobial peptides against commensal microbiota<sup>95</sup>. According to a mathematical model proposed by Tusco et al., host-pathogen co-evolution could have been the driving force for the loss of the LIR motif in mammalian NEMO<sup>95</sup>.

LUBAC-mediated quality control of cellular protein aggregates shares some similarities with its role in anti-bacterial autophagy.

**Fig. 4 | In contrast to Q330X NEMO, WT NEMO is recruited to pathological protein aggregates and increases the abundance of MI-linked ubiquitin.** **a** In contrast to WT NEMO, Q330X NEMO is not present at aSyn aggregates. SH-SY5Y cells stably expressing aSyn A53T-GFP were transiently transfected with either HA-tagged WT NEMO (left panel) or HA-tagged Q330X NEMO (right panel). After 24 h, the cells were treated with aSyn A53T seeds, fixed 48 h after seeding, and analyzed by immunocytochemistry and fluorescence SR-SIM using an antibody against the HA-tag. Scale bar, 20  $\mu\text{m}$  (overview) and 10  $\mu\text{m}$  (inset). The graph displays the percentage of cells showing colocalization of WT NEMO or Q330X NEMO with aSyn aggregates per field of view. Data are shown as mean  $\pm$  SEM based on 8 technical replicates within 2 biological replicates. At least 41 cells per condition were quantified. Statistics: non-parametric Mann–Whitney *U*-test. \*\*\* $p \leq 0.001$ . **b** Q330X NEMO is not recruited to Htt-Q97-GFP aggregates. SH-SY5Y cells were transiently transfected with Htt-Q97-GFP and either HA-tagged WT NEMO (left panel) or HA-tagged Q330X NEMO (right panel). Cells were fixed after 72 h and analyzed by immunocytochemistry and fluorescence SR-SIM using antibodies against the HA-tag. Scale bar, 10  $\mu\text{m}$  (overview) and 5  $\mu\text{m}$  (inset). **c** Q330X NEMO is not recruited to insoluble Htt-Q97-GFP aggregates. NEMO KO MEFs were transiently transfected with Htt-Q97-GFP and either WT HA-NEMO, Q330X HA-NEMO or K285R K309R HA-NEMO. After 72 h, the cells were lysed and the SDS-insoluble fractions were analyzed by a filter retardation assay. The cellulose acetate membranes were immunoblotted for Htt and NEMO (using an HA antibody). The input was immunoblotted using antibodies against HA and  $\beta$ -actin. **d** Q330X NEMO does not bind to MI-linked ubiquitin. HEK293T cells were transiently transfected with either WT HA-NEMO or Q330X HA-NEMO. After 24 h, the cells were lysed and lysates were incubated with recombinant MI-linked tetra-ubiquitin (4 $\times$ MI-ub) for 2 h at 4  $^{\circ}\text{C}$ . NEMO was immunoprecipitated using anti-HA beads. Immunoprecipitated NEMO was immunoblotted using antibodies against MI-linked ubiquitin. The input was immunoblotted for MI-linked ubiquitin, NEMO and  $\beta$ -actin. **e** Q330X NEMO is not MI-ubiquitinated upon TNF treatment or increased LUBAC expression. HEK293T cells

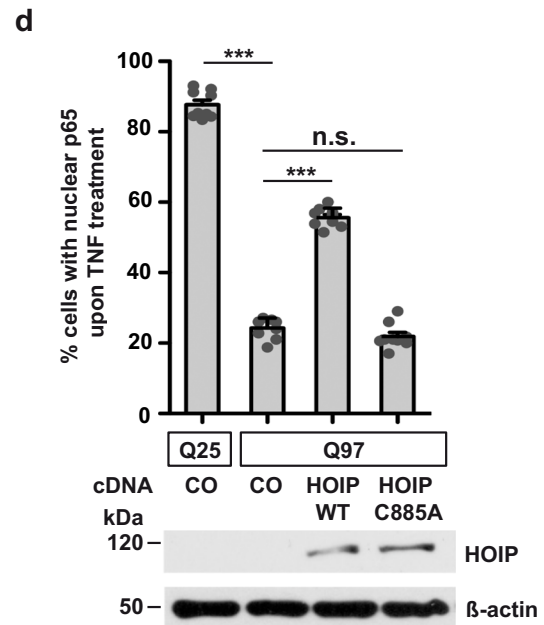
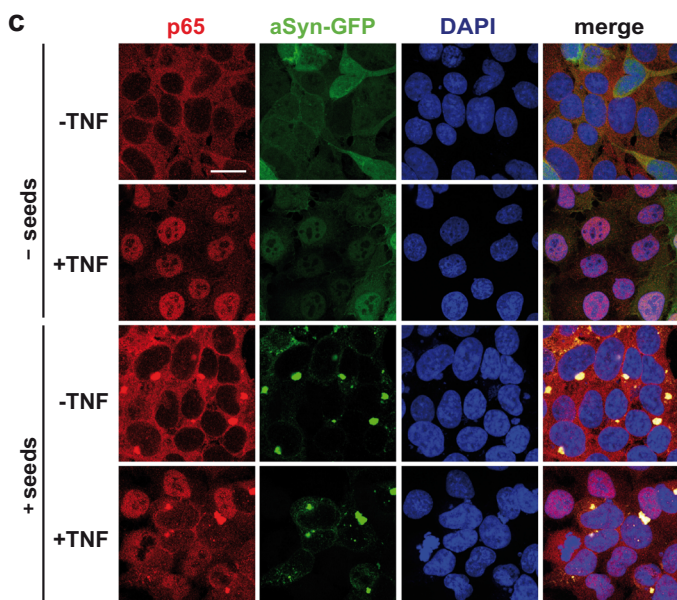
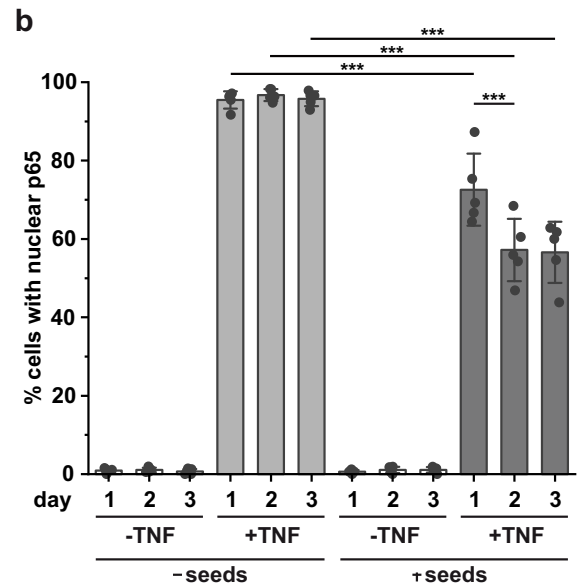
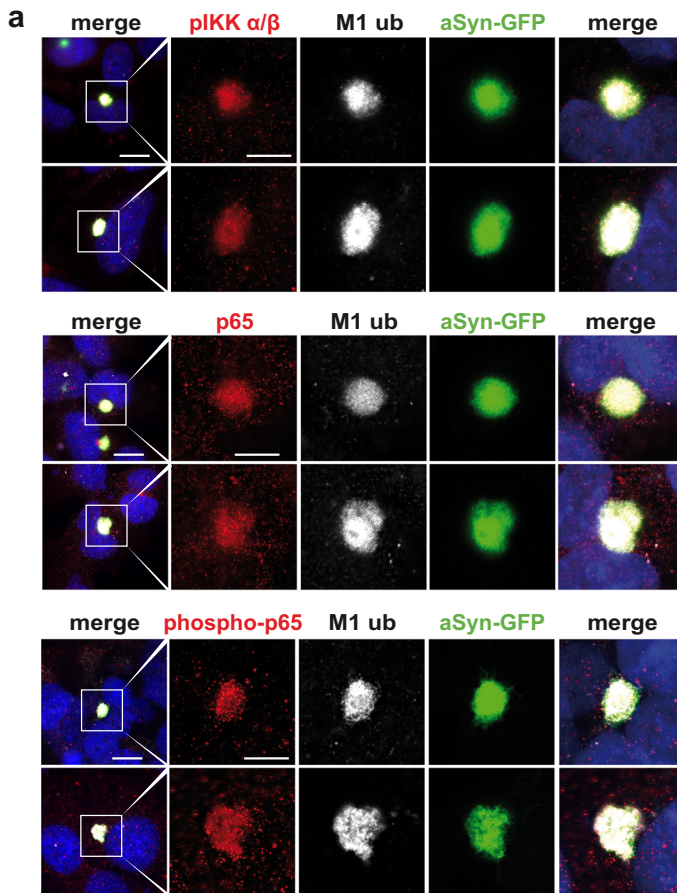
were transiently transfected with WT HA-NEMO or Q330X HA-NEMO  $\pm$  LUBAC (HOIP + HOIL-1L + SHARPIN) as indicated. After 24 h, one set of cells was treated with TNF (25 ng/ml, 30 min) to stimulate linear ubiquitination. After cell lysis under denaturing conditions, NEMO was immunoprecipitated using anti-HA beads. Immunoprecipitated NEMO was immunoblotted using antibodies against MI-linked ubiquitin. The input was immunoblotted for NEMO and  $\beta$ -actin. **f** In contrast to WT NEMO, Q330X NEMO does not co-immunoprecipitate with endogenous HOIP. HEK293T cells were transiently transfected with either WT HA-NEMO or Q330X HA-NEMO. After cell lysis, NEMO was immunoprecipitated using anti-HA beads. Anti-c-myc beads were used to control for nonspecific binding. Immunoprecipitated NEMO was immunoblotted for endogenous HOIP. The input was immunoblotted for HOIP, NEMO, and  $\beta$ -actin. **g, h** MI-ubiquitin chains at aSyn aggregates are increased by WT but not Q330X NEMO. CRISPR/Cas9 NEMO KO SH-SY5Y cells were transiently transfected with aSyn A53T-GFP and either WT NEMO or Q330X NEMO. One day after transfection, the cells were treated with aSyn A53T seeds, and fixed 48 h after seeding and analyzed by immunohistochemistry and fluorescence SR-SIM using antibodies against aSyn, MI-ubiquitin and NEMO. Colocalization of MI-ubiquitin, NEMO and aSyn aggregates (**g**) or MI-ubiquitin and aSyn aggregates (**h**) was quantified using the Pearson colocalization coefficient. **g** Data are displayed as mean  $\pm$  SEM,  $n = 16$  individual cells. Statistics: two-tailed Mann–Whitney *U*-test. \*\*\* $p = 0.0010$ . **h** Data are displayed as mean  $\pm$  SEM.  $n = 18$ , 23 individual cells. Statistics: two-tailed student's *t*-test. \*\*\* $p = 0.0003$ . **i** NEMO Q330X and NEMO D311N do not increase linear ubiquitination at Htt-polyQ aggregates. HEK293T cells were transfected with Htt-Q97-GFP and either wildtype HA-NEMO, HA-NEMO Q330X, or HA-NEMO D311N. The cells were lysed 72 h after transfection under denaturing conditions in 1.5 % (w/v) SDS. SDS-insoluble pellets were dissolved in formic acid. Formic acid-dissolved aggregates and the SDS-soluble fractions were analyzed by immunoblotting using antibodies against MI-linked ubiquitin, Htt, NEMO, and  $\beta$ -actin.

Bacteria that escape from the vacuolar compartment into the cytosol, such as *Salmonella* species, are coated by ubiquitin to restrict bacterial proliferation<sup>62–64</sup>. In this pathway, the RNF213 ubiquitin ligase ubiquitylates the bacterial outer membrane component lipopolysaccharide (LPS), which is a prerequisite for the subsequent recruitment of LUBAC<sup>64</sup>. HOIP binds to pre-existing ubiquitin at the bacterial surface and assembles MI-linked ubiquitin chains on bacterial membrane proteins or on ubiquitin moieties previously attached by RNF213. Linear ubiquitin chains then recruit Optineurin and NEMO to the bacterial surface, which both bind to MI-linked ubiquitin with high affinity via their UBAN domain. Whereas Optineurin induces selective autophagy to promote the clearance of bacteria, NEMO locally activates the IKK complex and thereby transforms the bacterial surface into an NF- $\kappa$ B signaling platform<sup>62,63</sup>. LUBAC-mediated aggrephagy differs from bacterial xenophagy in some substantial aspects. First, HOIP is recruited to cytosolic bacteria via its NZF domain by pre-existing ubiquitin assembled by RNF213<sup>64</sup>, whereas VCP/p97 is required to recruit HOIP to misfolded proteins by an interaction of the PIM domain of VCP/p97 with the PUB domain of HOIP<sup>49</sup>. Second, Optineurin is required for anti-bacterial autophagy, whereas for the clearance of misfolded aSyn p62 plays a major role, though we cannot exclude an additional role of Optineurin. Third, NEMO is apparently dispensable for bacterial autophagy<sup>62</sup> and mitophagy<sup>74,96</sup>, but required for autophagic degradation of aSyn. This difference may be attributable to the fact that p62 is a key cargo receptor in aggrephagy. The increased abundance of p62 in the brain of the Q330X NEMO patient may reflect either a compensatory upregulation by transcription factors other than NF- $\kappa$ B, such as NRF2<sup>97</sup>, or an accumulation of p62 due to a decreased autophagic flux.

Even though the role of LUBAC and NEMO in protein quality control seems to be independent of NF- $\kappa$ B signaling, impaired activation of the NF- $\kappa$ B prosurvival pathway may contribute to the toxicity of protein aggregates. Whereas prolonged and excessive NF- $\kappa$ B activation is associated with inflammation, constitutive NF- $\kappa$ B

signaling in neurons regulates synaptic plasticity and neuronal viability<sup>98–102</sup>. Moreover, induced NF- $\kappa$ B activation protects from neuronal cell death in various stress conditions<sup>102–105</sup>. Of note, several neurotrophic proteins, such as NGF, BDNF, and GDNF, signal via NF- $\kappa$ B to promote neuronal viability<sup>106–110</sup>. Our data indicate that similar to intracellular bacteria, an NF- $\kappa$ B signaling platform is assembled at aSyn aggregates. However, this signaling platform is not functional, since p65 seems to be sequestered and trapped at the aggregates so that not even an additional NF- $\kappa$ B-activating stimulus, like TNF, promotes nuclear translocation of p65. Thus, prosurvival signals cannot efficiently be transduced via NF- $\kappa$ B in cells with aSyn or Htt-polyQ aggregates. It is noteworthy in this context that our study revisits an earlier finding linking NEMO to PD. We previously discovered that linear ubiquitination of NEMO is a prerequisite for Parkin to prevent stress-induced neuronal cell death. This activity of Parkin was associated with adding K63-linked ubiquitin to NEMO, suggesting that Parkin can act as a priming E3 ligase for subsequent modification of NEMO by LUBAC<sup>111,112</sup>. Whether Parkin also plays a role in LUBAC-mediated protein quality control is an interesting question to be addressed in further studies.

Finally, our study adds to the notion that different neurodegenerative diseases share common pathways. The accumulation of various proteins linked to neurodegeneration in the brain of the Q330X NEMO patient reflects a general neuronal proteostasis dysregulation, which at least partially can be explained by defective p62-mediated selective autophagy. The presence of  $\alpha$ -synuclein, tau, and TDP-43 aggregates has also been reported in some patients with *OPTN* mutations affecting the UBAN domain of Optineurin, which binds linear ubiquitin chains<sup>113</sup>. Thus, neurodegeneration in these patients may also be linked to defective protein quality control downstream of LUBAC. Shared pathological mechanisms related to proteostasis dysregulation may entail specific targets for disease-modifying strategies. Further studies need to address whether the linear ubiquitination machinery can be exploited for therapeutic approaches.



**Methods**

**Ethical statement**

Research performed for this study complies with all ethical regulations of the respective local authorities the Charité Universitätsmedizin Berlin (Clinical Ethics Committee), and the Institute for Neuropathology, University Medical Center Hamburg-Eppendorf (Clinical Ethics Committee), Hamburg, Germany. *Post mortem* brain tissue from the

index case with the NEMO mutation and age-matched controls from the same brain regions were obtained from the Autopsy Service in the Department of Pathology at the University of California San Francisco. Brain tissue samples were collected after informed consent was obtained from the patient or their families, in accordance with guidelines put forth in the Declaration of Helsinki. Autopsy consent and all protocols were approved by the Human Gamete, Embryo, and

**Fig. 5 | A local NF- $\kappa$ B signaling platform is assembled at aSyn aggregates that does not promote nuclear translocation of p65.** **a** IKK $\alpha$ / $\beta$  and p65 are recruited to aSyn aggregates. SH-SY5Y cells stably expressing aSyn A53T-GFP were treated with aSyn A53T seeds, fixed on day 3 after seeding, and analyzed by immunocytochemistry and fluorescence SR-SIM using antibodies against phospho-IKK $\alpha$ / $\beta$ , p65, phospho-p65, and MI-linked ubiquitin. Scale bar, 10  $\mu$ m (overview) and 5  $\mu$ m (inset). **b, c** Assembling of an NF- $\kappa$ B signaling platform at aSyn aggregates does not result in p65 nuclear translocation and impairs TNF-induced NF- $\kappa$ B activation. **b** Samples were prepared as described in a, treated with TNF for 15 min (25 ng/ml) on day 1, 2, and 3 after seeding, fixed and quantified for nuclear translocation of p65 by immunocytochemistry and fluorescence microscopy using antibodies against p65. For the seeded samples, only cells with aSyn aggregates were used for quantification. Data represent the mean  $\pm$  SD of five independent experiments. Statistics:

One-way ANOVA followed by Tukey's multiple comparison test. \*\*\* $p \leq 0.001$ . **c** Representative immunofluorescence images of the experiment described in b (day 2 after seeding). Scale bar, 20  $\mu$ m. **d** TNF-induced p65 nuclear translocation is impaired in cells with Htt-polyQ aggregates. SH-SY5Y cells were transiently transfected with GFP-tagged Htt-25Q or Htt-Q97 and either vector (co), wildtype HOIP or catalytically inactive C885A HOIP, as indicated. On day 3 after transfection, the cells were treated with TNF (20 ng/ml, 20 min), and nuclear translocation of p65 was analyzed as described in (b). Expression of HOIP was analyzed by immunoblotting, actin was used as input control. Data represent the mean  $\pm$  SD of three independent experiments each performed in triplicates. At least 600 transfected cells were assessed per condition. Statistics: One-way ANOVA with Tukey's Multiple Comparison posthoc test; \*\*\* $p \leq 0.001$ .

Stem Cell Research Committee and the Institutional Review Board (IRB) at UCSF.

### Human brain sections

*Post mortem* brain samples from the Q330X NEMO patient, from DLBD patients and from respective controls were provided by the Department of Pathology, University of California, San Francisco, California, USA. PD brain samples were provided by the Charité Universitätsmedizin Berlin, Germany. *Post mortem* brain samples of frontal isocortex from neuropathologically confirmed AD, DLBD, FTLD and tauopathy patients were obtained from the Institute of Neuropathology, University Medical Center Hamburg-Eppendorf, Hamburg, Germany. Available data are listed in the Supplementary Table 1.

### Genetic analyses

For whole-genome sequencing (WGS) performed at CENTOGENE GmbH, genomic DNA was fragmented by sonication, and Illumina adapters were ligated to the generated fragments for subsequent sequencing on the HiSeqX platform (Illumina Inc., San Diego, CA). The achieved average coverage depth was at least 30x. Data analysis included base calling, de-multiplexing, and alignment to the hg19 human reference genome (Genome Reference Consortium GRCh37). The WGS finding was confirmed by Sanger sequencing of the relevant IKBKG exon on a ABI 3500xL Genetic Analyzer (Applied Biosystems) and analyzed using GeneMapper software (Applied Biosystems). The sequence variant nomenclature followed the standard Human Genome Variation Society guidelines (<http://varnomen.hgvs.org/>). Variants were classified according to the guidelines of the American College of Medical Genetics (ACMG)<sup>114</sup>. Written informed consent to participate in this study was provided. In addition, we obtained consent from the husband of the deceased patient to publish information that identifies individuals (including three or more indirect identifiers).

### DNA constructs

The following constructs were described previously: human HOIP, HOIL-1L, SHARPIN, HA-HOIP, HOIL-1L-HA, SHARPIN-HA, HA-HHARI, FLAG-NEMO WT, FLAG-NEMO D311N, HA-IKK $\beta$ , mCherry, NF- $\kappa$ B-luciferase reporter<sup>111</sup>; HA-HOIP C885A, Htt-Q25-GFP, Htt-Q97-GFP<sup>49</sup>; p62 and p62 $\Delta$ UBA<sup>12</sup>. HA-NEMO WT and HA-NEMO D311N were generated using the following primers: HA-NEMO-fwd: 5'-ATATGGATCC AATAGGCACCTCTGGAAGAGC-3', HA-NEMO-rev: 5'-ATATGCGGCCGC TACTCAATGCACTCCATGACATG-3'. The amplified fragment was digested with BamHI and NotI and cloned into pcDNA3.1-N-HA. HA-NEMO Q330X was generated using the following primers: HA-NEMO Q330X-fwd: 5'-ATAT GGATCC AATAGGCACCTCTGGAAGAGC-3', HA-NEMO Q330X-rev: 5'-ATATGCGGCCGCCTCACAGGAGCTCCTTCTTC TCGG-3'. The amplified fragment was digested with BamHI and NotI and cloned into pcDNA3.1-N-HA. FLAG-NEMO Q330X was generated using the following primers: FLAG-NEMO Q330X-fwd 5'- GCGC AAGCTT ATGGACTACAAGGATGATGACAAG-3', FLAG-NEMO

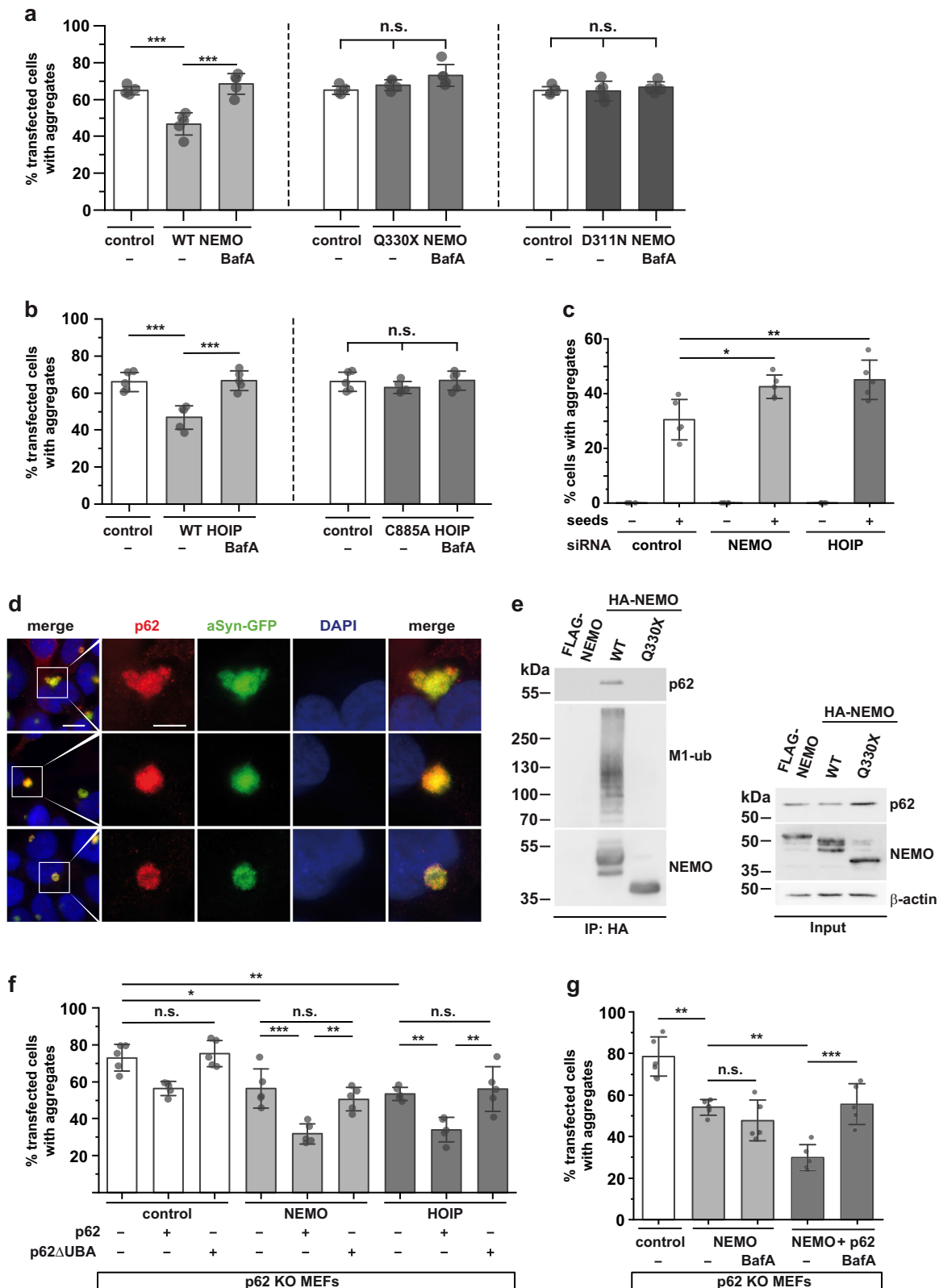
Q330X-rev 5'- ATAT TCTAGA CTACAGGAGCTCCTTCTTCTCGGC-3'. The amplified fragment was digested with HindIII and XbaI and cloned into pEF4 -N-FLAG. HA-IkB $\alpha$  was generated using the following primers: HA-IkB $\alpha$ -fwd: 5'- ATAT GGATCC ACCGAGGACGGGGACTCG-3', HA-IkB $\alpha$ -rev: 5'- ATAT GCGGCCGC CTATAACGTCAGACGCTGGCC-3'. The amplified fragment was digested with BamHI and NotI and cloned into pcDNA3.1-N-HA. p62 $\Delta$ UBA-HA (AA 1-388) was generated using the following primers: p62 $\Delta$ UBA-HA-fwd: 5'- ATAT GAATTC GCCACC ATG GCG TCG CTC ACC GTG-3', p62 $\Delta$ UBA-HA-rev 5'- TATAGCGGCCGC T GGC GGG AGA TGT GGG TAC-3'. The amplified fragment was digested with EcoRI and NotI and cloned into pcDNA3.1-C-HA. aSyn A53T-GFP was generated using the following primers:  $\alpha$ -Synuclein A53T-eGFP-fwd: 5'- ATAT AAGCTT GCCACC ATG GAT GTA TTC ATG AAA GGA C-3',  $\alpha$ -Synuclein A53T-eGFP-rev: 5'- ATATGCGGCCGCCTTCAGGTTCCG-TAGTC-3'. The amplified fragment was digested with HindIII and NotI and cloned into pcDNA3.1-C-eGFP.

### Cell lines

HEK293T cells (CRL-1573; American Type Culture Collection) were cultured in Dulbecco's modified Eagle's medium (DMEM) supplemented with 10% (v/v) fetal bovine serum (FBS) and 100 IU/ml penicillin 100  $\mu$ g/ml streptomycin sulfate. SH-SY5Y (DSMZ number ACC 209), were cultured in Dulbecco's modified Eagle's medium F-12 (DMEM/F-12) supplemented with 15% (v/v) fetal bovine serum (FBS), 100 IU/ml penicillin 100  $\mu$ g/ml streptomycin sulfate and 1% non-essential amino acids. Mouse embryonic fibroblasts (MEFs) derived from wildtype or NEMO KO mice<sup>115</sup> or p62 KO mice<sup>116</sup> were cultured in Dulbecco's modified Eagle's medium (DMEM) supplemented with 10% (v/v) fetal bovine serum (FBS) and 100 IU/ml penicillin 100  $\mu$ g/ml streptomycin sulfate.

### Generation of NEMO CRISPR/Cas9 knockout (KO) SH-SY5Y cells and HOIP CRISPR/Cas9 KO HeLa cells

sgRNAs (RNF31-24147982 AGGGUGUUGAGGUAGUUUCG; RNF31-24147993 GAGCCGUGGACAGGGUGUUG; IKBKG-154552050 UGUGAG AUGGUGCAGCCCAG; IKBKG-154552185 GAGGAGAAUCAAGAGCUC CG) were designed using the Synthego website ([www.design.synthego.com](http://www.design.synthego.com)). 1.5 nmol sgRNAs were rehydrated in 50  $\mu$ l nuclease-free 1 $\times$  TE buffer (10 mM Tris-HCl, 1 mM EDTA, pH 8.0) to a final concentration of 30  $\mu$ M (30 pmol/ $\mu$ l). sgRNA and recombinant CAS9 were delivered as ribonucleoprotein (RNP) complexes using a 4D-Nucleofector X-Unit (Lonza). Briefly, for the assembly of the RNP complexes, Cas9 2NLS and sgRNAs were combined in Nucleofector™ solution at a molar ratio of 9:1 sgRNA to Cas9 and incubated for 10 min at room temperature. The cells were resuspended at a concentration of 150,000 cells/5  $\mu$ l. 5  $\mu$ l of the cell suspension was added to the 25  $\mu$ l of pre-complexed RNPs for a total transfection volume of 30  $\mu$ l per reaction and transferred to Nucleofector cartridges. Nucleofection was performed according to the predefined protocol (CA-137 for SH-SY5Y- and CN-114 for HeLa cells) and cells were carefully resuspended in each well of the Nucleocuvette™ with 70  $\mu$ l of pre-warmed growth medium and



transferred to the pre-warmed 6-well and incubated in a humidified 37 °C/5% CO<sub>2</sub> incubator. After 24 h the medium was replaced.

For clone screening, the cells were split into two 6-well cell culture plates, and pools were analyzed by PCR and subsequent DNA sequencing. For this, primer pairs (HOIP\_fwd: AGTCCCACCCTCTCTCTAG, HOIP\_rev: TGTGACTGTAGCAACCTGGT, NEMO\_fwd: CCTGGAGCTAGGCCTTTTCA, NEMO\_rev: ACTTCTCCCCGCTAATCTG)

were ordered extending approx. 200–250 bp 3' and 5' of the sgRNA binding region. To perform cell pool or single clone sequencing analysis, genomic DNA was isolated using a genomic DNA extraction kit (Monarch Genomic DNA Purification Kit, New England Biolabs, Frankfurt am Main, Germany) and the PCR was optimized to yield a single amplicon. Following PCR product purification (NucleoSpin Gel and PCR Clean-up, Macherey-Nagel GmbH, Düren, Germany), the DNA

**Fig. 6 | NEMO decreases the number of cells with aSyn aggregates in a p62-dependent manner.** **a** WT NEMO but neither Q330X NEMO nor D311N NEMO decreases the number of cells with aSyn aggregates. SH-SY5Y cells stably expressing aSyn A53T-GFP were transiently transfected with either WT HA-NEMO, Q330X HA-NEMO, D311N HA-NEMO, or mCherry as a control and treated with aSyn A53T seeds 24 h after transfection. The cells were treated 16 h after seeding with Bafilomycin A1 (BafA, 25 nM). 40 h after seeding, the cells were fixed and analyzed by immunocytochemistry and fluorescence microscopy using anti-HA antibodies. The fraction of HA- or mCherry-positive cells containing aSyn-GFP aggregates was quantified. Data are shown as mean  $\pm$  SD based on 5 independent experiments. At least 750 cells per condition were quantified. Statistics were applied to the entire dataset. For better comparability, the control is shown for each NEMO construct. Statistics: One-way ANOVA followed by Tukey's multiple comparison test.  $***p \leq 0.001$ . **b** Catalytically active HOIP decreases the number of cells with aSyn aggregates. SH-SY5Y cells stably expressing aSyn A53T-GFP were transiently transfected with either WT HA-HOIP, catalytically inactive C885A HA-HOIP, or mCherry as a control, and treated as described in a. The fraction of HA- or mCherry-positive cells containing aSyn-GFP aggregates was quantified. Data are shown as mean  $\pm$  SD based on 5 independent experiments. At least 750 cells per condition were quantified. Statistics were applied to the entire dataset. For better comparability, the control is shown for each HOIP construct. Statistics: One-way ANOVA followed by Tukey's multiple comparison test.  $***p \leq 0.001$ . **c** NEMO and HOIP silencing increase the number of cells with aSyn-GFP aggregates. SH-SY5Y cells stably expressing aSyn A53T-GFP were transiently transfected with either NEMO- or HOIP-specific siRNAs, treated with aSyn A53T seeds as indicated, and fixed 48 h after seeding. The fraction of cells containing aSyn aggregates was quantified. Data are shown as mean  $\pm$  SD from 5 biological replicates. At least 750 cells per condition

were quantified. Statistics: One-way ANOVA followed by Bonferroni's multiple comparison test.  $*p \leq 0.05$ ,  $**p \leq 0.01$ . **d** p62 is present at aSyn aggregates. SH-SY5Y cells stably expressing aSyn A53T-GFP were treated with aSyn A53T seeds, fixed 72 h after seeding, and analyzed by immunocytochemistry and SR-SIM fluorescence microscopy using anti-p62 antibodies. Scale bar, 10  $\mu$ m (overview) and 5  $\mu$ m (inset). **e** p62 co-immunoprecipitates with WT NEMO but not with Q330X NEMO. HEK293T cells were transiently transfected with either WT HA-NEMO, Q330X HA-NEMO, or WT FLAG-NEMO to control for unspecific binding. After cell lysis, HA-tagged proteins were immunoprecipitated using anti-HA-beads. Immunoprecipitated proteins were immunoblotted using antibodies against p62, M1-linked ubiquitin, and NEMO. The input was immunoblotted for p62, NEMO, and  $\beta$ -actin. **f** NEMO and HOIP reduce the number of aSyn aggregates in a p62-dependent manner, which requires the UBA domain of p62. p62 KO MEFs were transiently transfected with aSyn A53T-GFP, HA-NEMO, HA-HOIP or mCherry as a control, and p62 or p62 $\Delta$ UBA, as indicated. One day after transfection, the cells were treated with aSyn A53T seeds, and fixed 48 h after seeding. The fraction of cells containing aSyn aggregates was quantified as described in a. Data are shown as mean  $\pm$  SD based on 5 individual experiments. Statistics: One-way ANOVA followed by Tukey's multiple comparison test.  $**p \leq 0.01$ ,  $***p \leq 0.001$ . **g** The p62-dependent effect of NEMO on aSyn aggregates is sensitive to lysosomal inhibition. p62 KO MEFs were transiently transfected with aSyn A53T-GFP and HA-NEMO, or HA-NEMO and p62, or mCherry as a control, as indicated. The next day, cells were treated with aSyn A53T seeds, and after 16 h treated with Bafilomycin A1 (BafA, 25 nM). 40 h after seeding, cells were fixed and the fraction of cells containing aSyn aggregates was quantified as described in a. Data are shown as mean  $\pm$  SD based on 5 individual experiments. Statistics: One-way ANOVA followed by Tukey's multiple comparison test.  $**p \leq 0.01$ ,  $***p \leq 0.001$ .

was sent for Sanger sequence analysis (Microsynth Seqlab GmbH, Göttingen, Germany). The KO efficiency of the cell pools and single colony clones was determined using the SYNTHGO ICE analysis website (<https://ice.synthego.com>). To isolate single KO clones, the KO cell pools were diluted to 1 cell/100  $\mu$ l and 5 cells/100  $\mu$ l, and the dilutions were distributed over several 96-well plates. 15–25 clones were grown from single cells and reanalyzed using the above-mentioned process. Finally, clones with a high KO score were amplified and KO efficiency was confirmed by immunoblotting.

### Expression and purification of recombinant proteins

Recombinant  $\alpha$ -synuclein expression and seeding was performed as described previously<sup>54,55</sup>. Briefly,  $\alpha$ -synuclein (aSyn) A53T encoded on a pT7-7 plasmid was transformed into *E. coli* strain BL21 (DE3). Bacteria were grown in Terrific Broth medium supplemented with ampicillin at 37 °C to a density of an A600 value of 0.8–1.0, and protein expression was induced by adding 1 mM IPTG for 4 h at 37 °C. Bacteria were harvested by centrifugation (6000 rcf, 20 min, 4 °C). Pellet was resuspended in high-salt buffer (750 mM NaCl, 10 mM Tris, pH 7.6, 1 mM EDTA, protease inhibitor tablet (Roche)) and lysed by sonication at 60% power using a probe sonicator (Branson sonifier 450) for a total time of 5 min (30 s pulse on, 30 s pulse off), followed by boiling of the sample for 15 min. After cooling on ice, the sample was centrifuged for 20 min at 6000 rcf. The supernatant was dialyzed overnight with 10 mM Tris, pH 7.6, 50 mM NaCl, 1 mM EDTA. Protein was concentrated with a 3.5 kDa MWCO Amicon ultracentrifuge filter device (Millipore). After filtering the protein through a syringe filter (0.45  $\mu$ m), the soluble proteins were separated by size exclusion chromatography on a Superdex 200 column (GE Healthcare Life Sciences). 40 2 ml fractions were collected using an ÄKTA chromatography system (GE Healthcare Life Sciences). Collected fractions were analyzed by SDS-PAGE using a 16% (w/v) polyacrylamide-gel followed by Coomassie staining/destaining. Fractions containing aSyn A53T were combined and dialyzed over night with 10 mM Tris, pH 7.6, 25 mM NaCl, 1 mM EDTA. On the next day, the combined fractions were subjected to anion-exchange chromatography on two connected 5 ml HiTrap Capto Q ImpRes (GE Healthcare Life Sciences) anion-exchange columns using a linear gradient, ranging from 25 mM NaCl to 1 M NaCl. Forty 2 ml fractions were collected using an

ÄKTA chromatography system (GE Healthcare Life Sciences). Collected fractions were analyzed by SDS-PAGE using a 16% (w/v) polyacrylamide-gel followed by Coomassie staining/destaining. Fractions containing aSyn A53T were combined and dialyzed over night with 50 mM Tris, pH 7.5, 150 mM KCl. Protein was concentrated with a 3.5 kDa MWCO Amicon ultracentrifuge filter device (Millipore) to a concentration of 5 mg/ml. Aliquots of 1 ml were stored at  $-80$  °C.

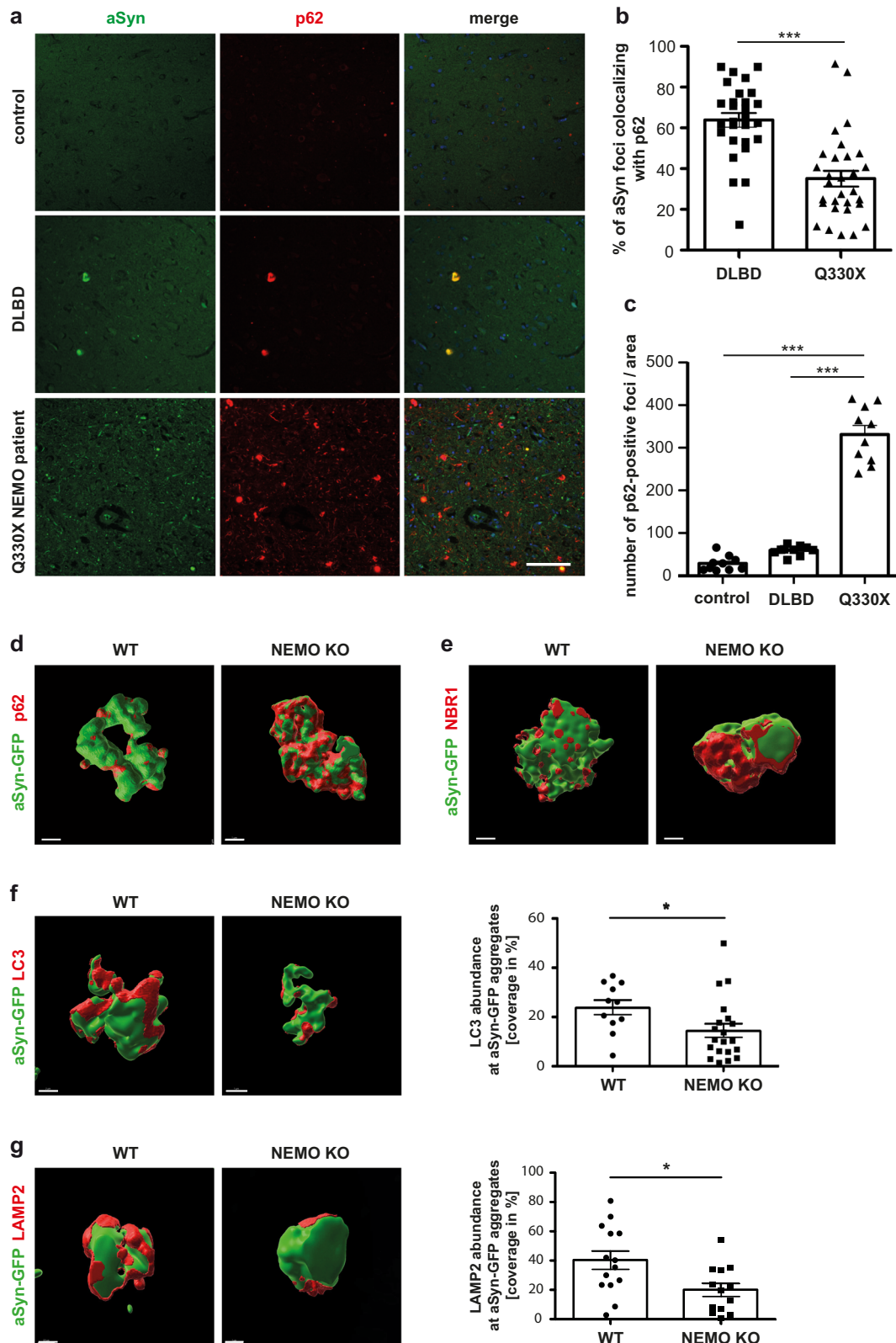
To prepare recombinant seeds for the induction of aSyn aggregates in SH-SY5Y cells stably expressing aSyn A53T-GFP, an aliquot containing 1 ml aSyn A53T with a concentration of 5 mg/ml was thawed on ice and centrifuged (20,000 rcf, 30 min, 4 °C). The supernatant was transferred into a new tube and incubated on a thermomixer for 24 h at 37 °C, 900 rpm. The sample was divided into 50  $\mu$ l aliquots and stored at  $-80$  °C until further use.

pET-Duet1-6xHis-mCherry-p62<sup>71</sup> was recombinantly expressed and purified from *E. coli* Rossetta (DE3) pLysS cells. Bacteria were grown in Luria broth (LB) medium until OD600=0.6, then induced with 0.3 mM isopropylthiogalactoside (IPTG) and grown at 20 °C for overnight. Harvested cells were resuspended in lysis buffer 50 mM 4-(2-hydroxyethyl)-1-piperazineethanesulfonic acid (HEPES) at pH 7.5, 500 mM NaCl, 10 mM imidazole, 2 mM MgCl<sub>2</sub>, 2 mM  $\beta$ -mercaptoethanol, complete protease inhibitor, and DNase I and lysed by French press. Lysates were cleared by ultracentrifugation at 40,000 *g* for 45 min at 4 °C. Supernatants were applied to Nickel-Nitrilotriacetic (Ni-NTA) His-Trap FF column (GE Healthcare) and 6xHis-tagged-mCherry-p62 was eluted via a stepwise imidazole gradient (50, 75, 100, 150, 200, and 300 mM). Protein-containing fractions were pooled and dialysed overnight at 4 °C in storage buffer containing 50 mM HEPES pH 7.5, 500 mM NaCl, 2 mM MgCl<sub>2</sub>, 2 mM  $\beta$ -mercaptoethanol. The protein was filtered using a 0.45  $\mu$ m syringe, aliquoted, and flash frozen until further use.

Wildtype NEMO-GFP and 4xMI-ubiquitin were expressed and purified as described previously<sup>50</sup>. 8xMI-ub was bought from Enzo Life Sciences.

### Induction of $\alpha$ -Synuclein aggregates by $\alpha$ -Synuclein A53T seeds in cultured cells and primary neurons

SH-SY5Y cells stably expressing aSyn A53T-GFP or MEFs transiently expressing aSyn- A53T-GFP were cultivated on glass coverslips



(Laboratory Glassware Marienfeld) for immunofluorescence analysis or on cell culture dishes for biochemical analysis. 24 h after plating, transient transfection, or gene silencing, freshly sonicated aSyn A53T seeds were added to the cells to a final concentration of 12.5  $\mu\text{g}/\text{ml}$  as follows:

50  $\mu\text{l}$  of aSyn A53T seeds were thawed at room temperature and added to 950  $\mu\text{l}$  Opti-MEM (Gibco) to obtain a concentration of 250  $\mu\text{g}/\text{ml}$ . Sonication was performed with a probe sonicator (Branson sonifier

450) for 3 min (30% power, 10 s intervals). Sonicated seeds were added to 960  $\mu\text{l}$  of Opti-MEM plus 40  $\mu\text{l}$  Lipofectamine 2000 (Invitrogen) in order to increase uptake of seeds by the cells, to a final concentration of 125  $\mu\text{g}/\text{ml}$ . After incubation for 15 min at room temperature, the seed solution was added to cells to obtain a final concentration of 12.5  $\mu\text{g}/\text{ml}$  per well in Opti-MEM. After 24 h the cells were either harvested, fixed for immunofluorescence experiments, or Opti-MEM was exchanged by Dulbecco's modified Eagle's medium F-12 (DMEM/F-12) supplemented



**Fig. 7 | p62 binds to aSyn aggregates in a NEMO-dependent manner. a, b, c** Colocalization of p62 and aSyn aggregates is decreased in the Q330X NEMO patient brain despite increased p62 expression. **a** Paraffin-embedded brain sections from control, DLBL (Dementia with Lewy Bodies) or the Q330X NEMO patient brain were analyzed by immunohistochemistry and fluorescence SR-SIM using antibodies against aSyn and p62. Scale bar, 200  $\mu\text{m}$ . **b** Foci staining positive for both aSyn and p62 were quantified in 28–30 fields of view per brain section. Data are shown as mean  $\pm$  SEM,  $n = 28/30$  individual cells. **c** Foci staining positive for p62 only were quantified in 10 fields of view per brain section. Data are displayed as mean  $\pm$  SEM from 10 fields of view. Statistics: Kruskal–Wallis test followed by Tukey's multiple comparison test.  $***p \leq 0.001$ . **d, e** Foci-like concentration of p62 and NBR1 at aSyn aggregates is reduced in NEMO-deficient cells. CRISPR/Cas9 NEMO KO or wildtype (WT) SH-SY5Y cells were transiently transfected with aSyn A53T-GFP. One day after transfection, the cells were treated with aSyn A53T seeds, fixed 48 h after seeding, and analyzed by immunohistochemistry and fluorescence SR-SIM using antibodies against p62 (**d**) and NBR1 (**e**). 3D-reconstructions were performed using the surface

module of Imaris 10.0.1 image analysis software. Scale bars, D/E: 1  $\mu\text{m}$ . **f, g** The abundance of LC3 and LAMP2 at aSyn aggregates is decreased in NEMO-deficient cells. CRISPR/Cas9 NEMO KO or WT SH-SY5Y cells were transiently transfected with aSyn A53T-GFP. One day after transfection, the cells were treated with aSyn A53T seeds, fixed 48 h after seeding, and analyzed by immunohistochemistry and fluorescence SR-SIM using antibodies against LC3 (**f**) and LAMP2 (**g**). 3D-reconstructions were performed using the surface module of Imaris 10.0.1 image analysis software. Coverage of aSyn-GFP aggregates by LC3 and LAMP2 was analyzed using the Imaris 10.0.1 surface modules and a surface-to-surface MatLab Plugin. The coverage of the reconstructed aSyn-GFP surface was quantified and plotted as percentage of the total aSyn-GFP aggregate surface for LC3 (**f**) and LAMP2 (**g**). Data are displayed as mean  $\pm$  SEM,  $n = 11/20$  individual cells for LC3 ( $*p = 0.0422$ ) and  $n = 14/13$  individual cells for LAMP2 ( $*p = 0.0143$ ). Statistics: two-tailed student's *t*-test.  $*p \leq 0.05$ . Scale bars, **f** 2  $\mu\text{m}$  (left panel), 1  $\mu\text{m}$  (right panel), **g** 0.5  $\mu\text{m}$  (left panel), 1  $\mu\text{m}$  (right panel).

with 15% (v/v) FCS, 1% (v/v) Penicillin/Streptomycin (Gibco) and 1% (v/v) minimum essential medium non-essential amino acids (Gibco), and cells were further grown for 24 to 48 h prior to harvesting or fixing.

For the induction of aSyn aggregation in primary cortical mouse neurons by aSyn A53T seeds, cells were plated on poly-L-lysine- and laminin-coated coverslips, and sonicated aSyn A53T seeds were added on DIV 5 to a final concentration of 1  $\mu\text{g}/\text{ml}$ . Primary neurons were fixed with 4% PFA 7 or 10 days after seeding and prepared for immunocytochemistry.

#### Detergent solubility assay

SH-SY5Y cells stably expressing aSyn A53T-GFP were grown in 3.5 cm dishes and harvested in cold PBS 24, 48, or 72 h after seeding with aSyn A53T seeds. Cells were lysed 10 min on ice in 1% (v/v) Triton X-100 in TBS supplemented with protease inhibitor (cOmplete, Roche) and phosphatase inhibitor (PhosStop, Roche). Samples were centrifuged (15 min, 20,000 rcf, 4 °C), the supernatants were transferred into new tubes, and 5 $\times$  Laemmli sample buffer was added (1% Triton X-100-soluble fraction). The pellets were washed two times with lysis buffer, solved in 1% (w/v) SDS in TBS, and boiled 15 min at 99 °C. In addition, DNA was sheared by passing the samples 15 times through a 23-Gauge needle. Finally, 5 $\times$  Laemmli sample buffer was added (1% SDS-soluble fraction). Equal amounts of the two fractions were used for analysis by immunoblotting using the indicated antibodies.

#### Immunocytochemistry

Cells were cultivated on glass coverslips (Laboratory Glassware Marienfeld). For some experiments, coverslips were coated with both poly-L-lysine (PLL) (Sigma) and laminin (Sigma) or PLL only. 24–72 h after seeding with aSyn A53T seeds, the cells were fixed for 10 min with 4% paraformaldehyde in PBS or Tris pH 7.4, and permeabilized and blocked in 0.2% (v/v) Triton X-100, 5% (v/v) goat serum in PBS or Tris for 2 h. Cells were stained with primary antibodies (Table 1) at a dilution of 1:100–1:1000 in 0.2% (v/v) Triton X-100, 5% (v/v) goat serum in PBS or Tris at 4 °C overnight, washed 3 $\times$  with PBS or Tris, and incubated with fluorescent dye-conjugated secondary antibodies Alexa Fluor 488, 555, or 647 (Thermo Scientific), at a dilution of 1:1000 for 1 h at room temperature. After extensive washing, cells were mounted in Fluoroshield G (Thermo Scientific) with DAPI (Sigma).

#### Immunohistochemistry

For peroxidase immunohistochemistry, paraffin-embedded brain sections (5  $\mu\text{m}$ ) were deparaffinized with xylene and ethanol and briefly washed with deionized water. Brain sections were cut from archived paraffin tissue blocks obtained during routine brain autopsy after whole-brain fixation in formalin for at least two weeks. Antigen retrieval through microwaving in 100 mM citrate buffer pH 6.0 was followed by blocking of endogenous peroxidase with 5%  $\text{H}_2\text{O}_2$  in

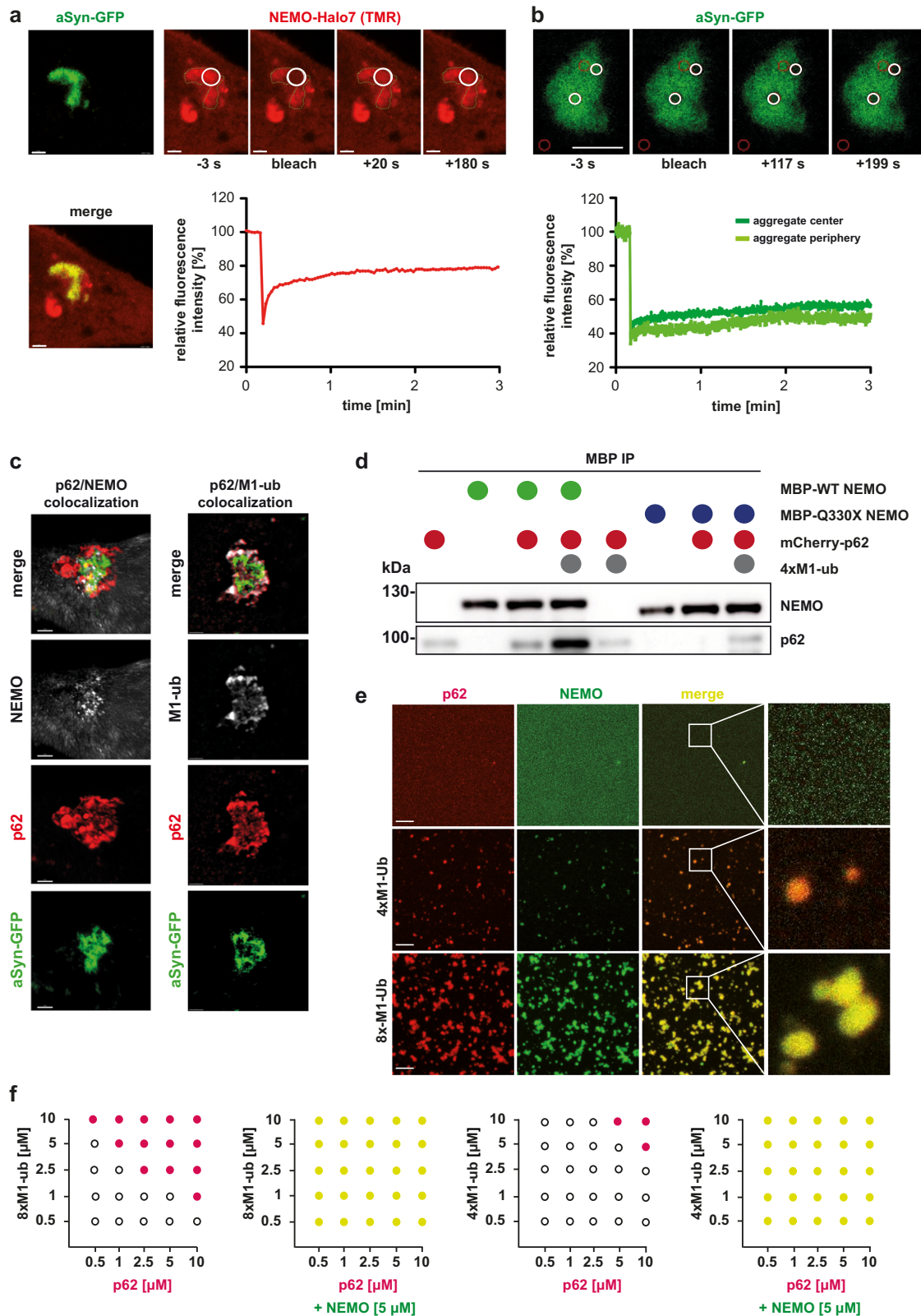
methanol. Then sections were transferred in PBS with 0.02% Brij35 and blocked with 2% FBS in PBS. Incubation with the primary antibody (Table 1) was performed overnight at 4 °C. After rinsing with 0.02 % Brij35 in PBS, antibody binding was detected and enhanced by DCS Super Vision 2 HRP-Polymer-Kit (DCS, Germany) using the chromogen DAB. Counterstaining with hematoxylin for cellular structures was performed. Microscopic images were obtained with a BX50 microscope and Cell-D software (Olympus).

For immunofluorescence histochemistry, paraffin-embedded human brain sections were deparaffinized, and antigen retrieval was performed as described above. Sections were blocked and permeabilized with 10% (v/v) goat serum, 0.3% (v/v) Triton X-100 in PBS for 1 h. Primary antibodies at a dilution of 1:50 ( $\alpha$ -synuclein), 1:100 (Tau, TDP-43, MIUbi, and NEMO) or 1:250 (p62) in 10% (v/v) goat serum, 0.3% (v/v) Triton X-100 in PBS were incubated at 4 °C for 48 h. After the brain sections were washed 3 $\times$  with PBS and blocked with 2% (w/v) BSA in PBS for 1 h, they were incubated with fluorescent dye-conjugated secondary antibodies Alexa Fluor 488 and 555 (Thermo Scientific) at a dilution of 1:1000 in 2% (w/v) BSA in PBS at room temperature for 1 h. After extensive washing, sections were mounted with Prolong Gold including DAPI (Thermo Fisher Scientific). Confocal images were obtained using a Zeiss ELYRA PS.1 equipped with an LSM880 (Carl Zeiss, Oberkochen). Super-resolution and confocal images were processed using the ZEN2.1 software (Carl Zeiss, Oberkochen).

#### Fluorescence microscopy

Fluorescence microscopy was performed using a Zeiss ELYRA PS.1 system equipped with an LSM880 (Carl Zeiss, Oberkochen) and a 20 $\times$ /0.8, 63 $\times$ /1.4 oil or 100 $\times$ /1.46 oil immersion objective or a C2+ system (Nikon). Super-resolution images were generated by the Structured Illumination (SIM) technology using 405, 488, 561, and 647 nm widefield laser illumination. SIM confocal images were processed using the ZEN Black software (Carl Zeiss, Oberkochen), image data were exported using the ZEN Blue software for further use. For the analysis of stained human brain sections, laser scanning microscopy was performed using the 405, 488, 561, and 647 nm laser illumination set in individual channels to avoid cross-talk. The pinhole was adjusted to generate optical section of 2–5  $\mu\text{m}$ , the acquisition settings were kept constant throughout the experiment. For the analysis of p62 positive aSyn aggregates in human brain sections, a 2  $\times$  2 tile scan using the 20 $\times$ /0.8 objective acquired and subsequently stitched with ZEN Black software.

**Colocalization studies.** To investigate the colocalization of aSyn, NEMO and MI-ub, the respective cell lines were transiently transfected with pcDNA3.1 aSyn A53T-GFP and seeded with aSyn seeds as described above. After 48 h the cells were fixed and stained with the respective antibodies as described under Immunocytochemistry.



To quantify the colocalization of NEMO and aSyn, M1-ub and NEMO, and M1-ub and aSyn, samples were imaged with constant laser settings, and respective signal thresholds were set to specific signal intensities and kept constant throughout the experiment. A contour was drawn around each protein aggregate and the Pearson colocalization coefficient within the contour was plotted for each comparison.

**Fluorescence recovery after photobleaching (FRAP).** For FRAP analysis, the Halo tag was labeled by incubating the cells for 30 min with 2.5  $\mu\text{M}$  TMR dye and washing for 30 min with cell culture medium prior to live cell imaging. FRAP was performed by 5 consecutive bleaching pulses using the 561 nm laser at 100% intensity within a defined region of interest (white circle) at an aSyn-GFP protein aggregate (green outline). The measurement within the aSyn-GFP

**Fig. 8 | NEMO promotes the local concentration of p62 by co-condensation with M1-linked ubiquitin.** **a, b** NEMO forms a mobile phase at immobile aSyn aggregates. CRISPR/Cas9 NEMO KO HeLa cells were transiently transfected with aSyn A53T-GFP and NEMO-Halo7. One day after transfection the cells were incubated with aSyn A53T seeds for 48 h. **a** For labeling of the Halo tag, the cells were incubated for 30 min with 2.5  $\mu\text{M}$  TMR dye and washed for 30 min with cell culture medium prior to live cell imaging. Fluorescence recovery after photobleaching (FRAP) was performed by 5 consecutive bleaching pulses using the 561 nm laser at 100% intensity within a defined region of interest (white circles) at an aSyn-GFP aggregate (green). Fluorescence recovery was measured for 3 min and plotted as a percentage of baseline fluorescence. Scale bar, 1  $\mu\text{m}$  **b** aSyn-GFP aggregates were bleached at two independent positions at the aggregate center or aggregate periphery (white circles) using 5 consecutive bleaching pulses using the 488 nm laser at 100% intensity within defined regions of interest. Fluorescence recovery was measured for 3 min and plotted as a percentage of baseline fluorescence. Scale bar, 5  $\mu\text{m}$ . **c** p62 colocalizes with NEMO and M1-linked ubiquitin at aSyn aggregates. HeLa cells were transiently transfected with aSyn A53T-GFP. One day after transfection, the cells were treated with aSyn A53T seeds, fixed 48 h after seeding and analyzed by immunohistochemistry and fluorescence SR-SIM using anti-antibodies against p62, NEMO and M1-ubiquitin (all at endogenous expression). Shown are

representative images of p62 co-localizing with NEMO (left panel) and p62 co-localizing with M1-ubiquitin (right panel) at aSyn-GFP aggregates. Scale bar, 1  $\mu\text{m}$ . **d** The interaction of NEMO with p62 is enhanced in presence of linear ubiquitin chains. 2.5  $\mu\text{M}$  recombinant MBP-NEMO WT or Q330X and 2  $\mu\text{M}$  recombinant mCherry-p62 were incubated with or without 1  $\mu\text{M}$  recombinant linear tetra-ubiquitin (4 $\times$ M1-ub) with 25  $\mu\text{L}$  MBP affinity agarose beads. Proteins were immunoblotted using antibodies against p62, and NEMO. **e** p62 and NEMO co-condensate in the presence of M1-linked polyubiquitin. 2.5  $\mu\text{M}$  recombinant mCherry-p62 (red) mixed with 5  $\mu\text{M}$  recombinant wildtype NEMO-GFP (green) were supplemented with M1-linked ubiquitin to induce phase separation. Top lane: No M1-linked ubiquitin added. Middle lane: 2.5  $\mu\text{M}$  M1-linked tetra-ubiquitin (4 $\times$ M1-ub). Bottom lane: 1.0  $\mu\text{M}$  M1-linked octa-ubiquitin (8 $\times$ M1-ub). Shown are laser scanning microscopy images. Scale bar, 10  $\mu\text{m}$ . **f** NEMO reduces the threshold concentrations required for ubiquitin-dependent p62 phase separation. Phase diagrams depicting concentration-dependent phase separation of p62 and M1-linked octa- or tetra-ubiquitin (8 $\times$ M1-ub or 4 $\times$ M1-ub) with or without 5  $\mu\text{M}$  recombinant wildtype NEMO. p62 was incubated in presence of recombinant M1-linked ubiquitin at the concentrations indicated and analyzed by laser scanning microscopy. Black empty circles: no phase separation; red/yellow solid circles: phase separation.

**Table 1 | Antibodies used in this study**

Antibody	Source	Identifier
Mouse monoclonal anti-HA	BioLegend	Cat# 901502, RRID: AB_2565007
Rabbit polyclonal anti-IKKBG/NEMO	Sigma-Aldrich	Cat# HPA000426, RRID: AB_1851572
Mouse monoclonal anti-IKK $\gamma$ /NEMO	Cell Signaling Technology	Cat#2695, RIDD: N/A, clone: DA10-12
Rabbit anti-IKK $\gamma$ /NEMO	Abcam	Ab178872
Rabbit monoclonal anti-linear ubiquitin	Millipore	Cat# MABS199, RRID: AB_2576212
Human monoclonal anti-linear ubiquitin	Genentech	clone: 1F11/3F5/Y102L, <sup>56</sup>
Mouse monoclonal anti-GFP	Thermo Fisher Scientific	Cat# 14-6674-82, RRID: AB_2572900
Mouse monoclonal anti- $\alpha$ -synuclein	BD Biosciences	Cat# 610787, RRID: AB_398108
Rabbit monoclonal anti- $\alpha$ -synuclein, (phospho Ser129)	Abcam	Cat# ab51253, RRID: AB_869973
Mouse anti- $\alpha$ -synuclein	Santa Cruz Biotechnology	Sc-12767, RRID:AB_628318
Mouse anti-phospho-tau	Invitrogen	Cat# MN1020
Mouse anti-TDP-43	Proteintech	Cat# 60019-2-Ig
Rabbit anti-TDP-43	Proteintech	Cat#12892-1-AP
Mouse monoclonal anti $\beta$ -actin	Sigma-Aldrich	Cat# A5316, RRID: AB_476743
Rabbit polyclonal anti-phospho-IKK $\alpha/\beta$ (Ser176, Ser180)	Thermo Fisher Scientific	Cat# 710676, RRID: AB_2532752
Rabbit monoclonal anti-NF- $\kappa$ B p65	Cell Signaling Technology	Cat# 8242, RRID: AB_10859369
Rabbit monoclonal anti-phospho-NF- $\kappa$ B p65 (Ser536)	Thermo Fisher Scientific	Cat# MA5-15160, RRID: AB_10983078
Rabbit polyclonal anti-p62 / SQSTM1	MBL International	Cat# PM045, RRID: AB_1279301
Rabbit polyclonal anti-p62	Proteintech	Cat# 18420-1-AP, RRID:AB_10694431
Mouse monoclonal anti-beta III Tubulin - Neuronal Marker	Abcam	Cat# ab78078, RRID: AB_2256751
Rabbit polyclonal anti-HOIP	Bethyl	Cat# A303-560A, RRID: AB_10949139
Mouse monoclonal anti-Ik $\beta$	Cell Signaling Technology	Cat# 4814, RRID: AB_390781
Mouse monoclonal anti-DYKDDDDK Tag (FLAG)	Cell Signaling Technology	Cat# 8146, RRID: AB_10950495
Rabbit monoclonal anti-cleaved caspase-3	Cell Signaling Technology	Cat# 9664, RRID: AB_2070042
Rabbit polyclonal anti-PARP	Cell Signaling Technology	Cat# 9542
Rabbit monoclonal anti-K63 Ubiquitin	Millipore	Cat# 05-1308, RRID: AB_1587580
Rabbit monoclonal anti-K48 Ubiquitin	Cell Signaling Technology	Cat# 8081, RRID: AB_10859893
Mouse monoclonal anti-Ubiquitin	Santa Cruz Biotechnology	Cat# sc-8017, RRID:AB_628423
Mouse monoclonal anti-LAMP2	Santa Cruz Biotechnology	Cat# 18822, RRID: AB_626858
Rabbit monoclonal anti-NBR1	Cell Signaling Technology	Cat# 9891, RRID: AB_10949888
Rabbit polyclonal anti-LC3	Proteintech	Cat# 14600-1-AP, RRID:AB_2137737
Mouse monoclonal anti-LC3	Nanotools	Cat# 0260-100/LC3-2G6, RRID:AB_2943418
Rabbit polyclonal anti-huntingtin Exon1	Enzo Life Sciences	Cat# BML-PW0595-0025, RRID: AB_2051651

aggregates was performed using 5 consecutive bleaching pulses with the 488 nm laser at 100% intensity at the indicated regions of interest (white circle). Fluorescence recovery was measured every 20 ms for 3 min and plotted as a percentage of baseline fluorescence.

**3D-image reconstruction and surface coverage analysis.** To investigate the coverage by LC3 and LAMP2 and the spatial localization of p62 and NBR1 at aSyn protein aggregates, image acquisition was performed using a Zeiss Elyra7 equipped with the SIM<sup>2</sup> module. Images stacks of 3–8  $\mu\text{m}$  in z were collected using the Leap-function and the minimal interval. Following the SIM conversion by ZEN 3.0 black, images were imported into Imaris 10.0.3 image analysis software. 3D-surfaces of aSyn aggregates and the respective antibody signal were reconstructed using the Surface module in batch mode. Surface-to-surface contacts sites were analyzed using a MatLab Plugin (Imaris website modules). The coverage of the reconstructed aSyn aggregate surface by the respective antibody signal was quantified and plotted as the percentage of the total aSyn-GFP aggregate surface.

**Analysis of condensate formation.** Fluorescent imaging laser scanning microscopy was performed using an LSM880 (Carl Zeiss, Oberkochen) with a 63 $\times$  oil immersion objective. A 63 $\times$  NA 1.4 oil immersion objective was used to record a z-stack of 67.5  $\times$  67.5  $\times$  10 and 0.330  $\mu\text{m}$  for each optical section. The argon laser power was set to 0.006% at 488 nm with pixel dwell time of 5.71  $\mu\text{s}$ . During all measurements, laser power, gain, and field of view were kept constant. The Z-stacks were then processed to obtain maximum intensity projections.

### Immunoprecipitations

Cells were lysed in 1% (v/v) Triton X-100 in PBS supplemented with 30 mM NEM (Sigma), protease inhibitor (cOmplete, Roche), and phosphatase inhibitor (PhosStop, Roche). The lysates were cleared by centrifugation (20,000  $\times g$ , 4  $^{\circ}\text{C}$ , 15 min). Samples were incubated overnight with anti-HA magnetic beads (Thermo Scientific) or for 5 h with GFP-Trap magnetic agarose (Chromotek) at 4  $^{\circ}\text{C}$  under rotation. Beads were washed five times with 1% (v/v) Triton X-100 in PBS. Immunopurified proteins were eluted by adding 2 $\times$  Laemmli sample buffer and boiling for 10 min at 95  $^{\circ}\text{C}$ . Samples were analyzed by immunoblotting using the indicated antibodies (Table 1).

### p65 translocation assay

SH-SY5Y cells stably expressing  $\alpha$ -Synuclein A53T-GFP were plated on cover slips, and after 24 h they were treated with  $\alpha$ -Synuclein A53T seeds (+ seeds) or PBS as a control (–seeds). One, two, and three days post-seeding, cells were treated with 25 ng/ml TNF (PeproTech) for 15 min as indicated and fixed with PFA. Samples were analyzed by immunocytochemistry using an antibody for p65. Nuclear translocation was quantified using the green, red, and DAPI channel of a fluorescence microscope (Nikon Eclipse E400).

### Quantification of aSyn A53T-GFP aggregates

After preparation of the samples on coverslips, they were analyzed using the green, red, and DAPI channel of a fluorescence microscope (Nikon Eclipse E400). Cells containing aggregates or fibrillar structures of aSyn A53T-GFP were counted positive, cells with neither aggregates nor fibrillar structures but with cytosolic and nuclear GFP staining were counted negative. When plasmids were transiently transfected during sample preparation, only cells positive for the transfected construct were considered. For quantification of the percentage of cells with aggregates five independent experiments were performed, and at least 150 cells were analyzed per condition for each replicate.

### Analysis of SDS-insoluble Htt-Q97 proteins

HEK293T cells transfected with the indicated plasmids were grown on 10 cm dishes. Three days after transfection, the cells were harvested

and lysed under denaturing conditions in TEX buffer (70 mM Tris-HCl pH 6.8, 1.5% SDS (w/v), 20% glycerol (v/v)), vortexed for 10 s, heated to 99  $^{\circ}\text{C}$ , and DNA was sheared by passing the samples 15 times through a 23-Gauge needle. Subsequently, DTT was added to the samples at a final concentration of 50 mM, the samples were boiled for 10 min at 99  $^{\circ}\text{C}$ , and centrifuged for 60 min (20,000 rcf, room temperature). The SDS-insoluble pellets were dissolved in 70  $\mu\text{l}$  100% formic acid by incubation of the samples for 40 min at 37  $^{\circ}\text{C}$  while shaking at 1000 rpm. Formic acid was evaporated overnight at 30  $^{\circ}\text{C}$  using a Speedvac system (Eppendorf). The remaining protein pellets were solved in Laemmli sample buffer and boiled for 10 min at 95  $^{\circ}\text{C}$ . SDS-insoluble, formic acid-dissolved aggregates were analyzed by immunoblotting using the M1-ubiquitin-specific antibody 1F11/3F5/Y102L.

### Filter retardation assay

To detect Htt aggregates, transfected cells were lysed in 1% (v/v) Triton X-100, 50 mM  $\text{MgCl}_2$  and 0.2 mg/ml DNase I in PBS. After centrifugation (180,000  $\times g$  for 30 min at 4  $^{\circ}\text{C}$ ) the pellet was resuspended in 2% SDS in 100 mM Tris (pH 7.0). After 1 h incubation at room temperature the homogenates were diluted 1:5 in 100 mM Tris (pH 7.0) and filtered through a cellulose acetate membrane with 0.2  $\mu\text{m}$  pore size (GE) using a Slot Blot Blotting Manifold (Hoeffer).

### Sedimentation assay

An aliquot of both aSyn A53T seeds and aSyn A53T monomers was thawed at room temperature. 10  $\mu\text{l}$  of each sample was centrifuged for 10 min at 20,000 rcf, respectively. The supernatant was transferred into a new tube and 10  $\mu\text{l}$  of 2 $\times$  Laemmli sample buffer was added (sup). The pellets were resuspended in 200  $\mu\text{l}$  PBS and centrifuged again (20,000 rcf, 10 min). Supernatants were discarded and 10  $\mu\text{l}$  PBS and 10  $\mu\text{l}$  2 $\times$  Laemmli sample buffer were added to the pellets (pellet). Sup and pellet fractions of both seeds and monomeric aSyn A53T were analyzed by SDS-PAGE and Coomassie staining/destaining.

### Thioflavin T assay

An aliquot of both aSyn A53T seeds and aSyn A53T monomers was thawed at room temperature. For each sample 4 technical replicates were prepared: For each technical replicate either 5  $\mu\text{l}$  of seeds, monomeric aSyn A53T, or PBS were pipetted into a black 96-well plate (Berthold), respectively. Samples were incubated with 95  $\mu\text{l}$  of a 25  $\mu\text{M}$  Thioflavin T (Sigma–Aldrich) in PBS solution for 45 min at room temperature. Fluorometry was performed using a microplate reader (Cytation 5, BioTek, excitation 442 nm, emission 485 nm).

### Atomic force microscopy (AFM)

AFM measurements were conducted on a Bruker Bioscope RESOLV, using Peak Force Tapping Mode at 2 kHz resonant frequency. For liquid AFM measurements a ScanAsyst Fluid+ probe from Bruker Nano was run at 0.5 nN setpoint and a peak force amplitude of 90 nm. Freshly cleaved MICA from PLANO was used as a substrate for in situ measurements. Beam alignment was done in the buffer solution. 4  $\mu\text{l}$  of the target solution was drop cast on the MICA substrate, shortly after (max. 10 s) the volume was filled with 2 ml buffer solution. For dry AFM measurements a ScanAsyst Air probe from Bruker Nano was run at 1.3 nN setpoint and a peak force amplitude of 150 nm. A silicon wafer from PLANO was used as a substrate for dry measurements. 4  $\mu\text{l}$  of the target solution was spin coated on the Si-substrate (5.59  $\times g$ ) and air counter flux.

### Dynamic light scattering (DLS)

DLS measurements were performed on a Malvern Instruments Zetasizer Ultra (633 nm laser source), in a 20  $\mu\text{l}$  quartz cuvette (ZEN2112). The displayed data were recorded over three cycles in back-scattering mode. The total acquisition time was 2 s. Attenuation and position were fixed by the device automatically. The refractive index and absorbance of polystyrene was used.

### Analysis of proteotoxic stress

**Immunocytochemistry.** MEFs were cultivated on glass coverslips (Laboratory Glassware Marienfeld). 24 h after seeding, cells were heat stressed at 42 °C for 1 h or treated with 0.5 μM MG-132 for 48 h or 100 nM BafA1 for 48 h. Cells were fixed for 15 min with 4 % paraformaldehyde in PBS pH 7.4 and permeabilized with 0.5% (v/v) Triton X-100, 3 mM EDTA pH 8.0, and 5% goat serum in PBS for 30 min at room temperature and then stained with Proteostat® (Enzo Life Sciences, Inc.) at a dilution of 1:2000 in 1× assay buffer (ENZO) for 20 min. Cells were then mounted in Fluorshield with DAPI (Sigma). Fluorescence microscopy was performed using a Zeiss ELYRA PS.1 equipped with an LSM880 (Carl Zeiss, Oberkochen) with a 63 × oil immersion objective. Super-resolution images were generated by the Structured Illumination (SIM) technology. SIM confocal images were processed using the ZEN2.1 software (Carl Zeiss, Jena).

**Trypan blue dye exclusion.** Cells were seeded in a 6-well dish at a density of ~500,000 cells. After 24 h, cells were either heat stressed at 46 °C for 1 h or treated with MG-132 for 16 h (2 μM), or 24 h (2 μM), or 48 h (0.5 μM) or treated with BafA1 for 16 h (500 nM), or 24 h (500 nM), or 48 h (100 nM) and trypsinized. The cell suspension was centrifuged for 5 min at 100 × g and the cell pellets were resuspended in PBS. One part of cell suspension was mixed with one part of trypan blue dye. Trypan blue dye only permeates damaged cell membranes. Therefore, the unstained (viable) and stained (nonviable) cells were counted by using a hemocytometer. To obtain the total number of viable cells per ml of aliquot, the total number of viable cells were multiplied by 2 (the dilution factor for trypan blue). To obtain the total number of cells per ml of aliquot, the total number of viable and nonviable cells were added and multiplied by 2. The percentage of viable cells were calculated as follows: Cell viability (%) = (total number of viable cells per ml of aliquot/total number of cells per ml) \*100.

**Immunoblotting.** Proteins were size-fractionated by SDS-PAGE (16% or 8% polyacrylamide) and transferred to nitrocellulose by electroblotting. The nitrocellulose membranes were blocked with 5% non-fat dry milk in TBST (tris-buffered saline (TBS) containing 0.1% Tween 20) for 30 min at room temperature and subsequently incubated with the primary antibody against Poly (ADP-ribose) polymerase (PARP) or active caspase-3 in TBST for 16 h at 4 °C. After extensive washing with PBST, the membranes were incubated with horseradish peroxidase-conjugated secondary antibody for 1 h at room temperature. Following washing with PBST, the antigen was detected with the enhanced chemiluminescence detection system.

### Pull-down assay for protein-protein interaction

2.5 μM recombinant NEMO and 2 μM recombinant p62 were incubated with or without 1 μM recombinant linear tetra-ubiquitin chains with 25 μL MBP affinity agarose beads (Chromotek) for 4 h at 4 °C on rotation. The beads were pre-equilibrated in native buffer containing 50 mM HEPES pH 7.4, 150 mM NaCl, 1 mM EDTA, 1 mM EGTA, 1% Triton X-100, 10% glycerol, 25 mM NaF, 10 μM ZnCl<sub>2</sub> supplemented with protease inhibitor (cOmplete, Roche) and N-ethylmaleimid (Sigma) in PBS. After 4 h, the beads were washed 5 times with the same native buffer and then boiled in 2× Laemmli sample buffer for 8 min at 95 °C. Samples were analyzed by immunoblotting using the indicated antibodies (Table 1).

### Phase separation assay

Protein aliquots were thawed on ice. Using Vivaspin 500 columns with 30 or 10 kDa molecular weight cut off (Sartorius Stedim Biotech), the buffer was exchanged to 10 mM Tris, pH 7.4, 1 mM DTT by centrifuging five to eight times for 9 min at 12,000 g, 4 °C. After buffer exchange, protein was collected and finally centrifuged at 20,000 g for 10 min at

4 °C to remove aggregates. The final protein concentration was determined by NanoDrop 2000. TEV protease was added to the samples and incubated 1 h for complete cleavage of MBP and 6xHis before microscopy. After the reaction, 10 μl of reaction mix was spotted on ibidi coverslip bottom dishes. The samples were then imaged as maximum intensity projection of a z-stack obtained using laser scanning microscopy.

### Quantification and statistical analysis

Data represent the mean ± SD or SEM, *n* numbers are indicated in the figure legends. For the quantification analysis in which manual counting was used, not all experiments were performed in a blinded manner. All statistical analyses were performed by using GraphPad PRISM (Version 5; San Diego, CA, USA). To check for Gaussian distribution of the data, the Kolmogorov–Smirnov test was applied. Based on the outcome of the test, appropriate parametric and non-parametric tests were chosen. For the comparison of two independent parametric datasets, the student's *t*-test was used. For the comparison of more than 2 parametric datasets, one-way ANOVA was applied. To correct for α-error inflation resulting from multiple comparisons, ANOVA was followed by the Tukey's post hoc multiple comparison tests. For the direct comparison of two non-parametric datasets, the Wilcoxon Mann–Whitney (*U*-test), and for the comparison of more than 2 non-parametric datasets, the Kruskal–Wallis test was used. Significance levels for all tests: \**P* ≤ 0.05; \*\**P* ≤ 0.01; \*\*\**P* ≤ 0.001. For the analysis of microscopic images, representative images are displayed; experiments were performed at least three times with similar results.

### Reporting summary

Further information on research design is available in the Nature Portfolio Reporting Summary linked to this article.

### Data availability

The authors declare that the data supporting the findings of this study are available within the article and its supplementary information files. Source data are provided with this paper. The whole-genome sequencing data generated in this study have been deposited in the NCBI Sequence Read Archive database under accession codes <http://www.ncbi.nlm.nih.gov/bioproject/1043442> and <https://www.ncbi.nlm.nih.gov/biosample/38340847>. Source data are provided with this paper.

### References

1. Kwon, Y. T. & Ciechanover, A. The ubiquitin code in the ubiquitin-proteasome system and autophagy. *Trends Biochem. Sci.* **42**, 873–886 (2017).
2. Johnston, H. E. & Samant, R. S. Alternative systems for misfolded protein clearance: life beyond the proteasome. *FEBS J.* **288**, 4464–4487 (2021).
3. Le Guerroue, F. & Youle, R. J. Ubiquitin signaling in neurodegenerative diseases: an autophagy and proteasome perspective. *Cell Death Differ.* **28**, 439–454 (2021).
4. Lei L., Wu Z., Winklhofer K. F. Protein quality control by the proteasome and autophagy: a regulatory role of ubiquitin and liquid-liquid phase separation. *Matrix Biol.* **100–101**, 9–22 (2020).
5. Pohl, C. & Dikic, I. Cellular quality control by the ubiquitin-proteasome system and autophagy. *Science* **366**, 818–822 (2019).
6. Yin, Z., Popelka, H., Lei, Y., Yang, Y. & Klionsky, D. J. The roles of ubiquitin in mediating autophagy. *Cells* **9**, 2025 (2020).
7. Bauer, B., Martens, S. & Ferrari, L. Aggrephagy at a glance. *J. Cell Sci.* **136**, jcs260888 (2023).
8. Adriaenssens, E., Ferrari, L. & Martens, S. Orchestration of selective autophagy by cargo receptors. *Curr. Biol.* **32**, R1357–R1371 (2022).

9. Sanchez-Martin, P. & Komatsu, M. p62/SQSTM1 - steering the cell through health and disease. *J. Cell Sci.* **131**, jcs222836 (2018).
10. Dikic, I. & Elazar, Z. Mechanism and medical implications of mammalian autophagy. *Nat. Rev. Mol. Cell Biol.* **19**, 349–364 (2018).
11. Vargas, J. N. S., Hamasaki, M., Kawabata, T., Youle, R. J. & Yoshimori, T. The mechanisms and roles of selective autophagy in mammals. *Nat. Rev. Mol. Cell Biol.* **24**, 167–185 (2023).
12. Bjorkoy, G. et al. p62/SQSTM1 forms protein aggregates degraded by autophagy and has a protective effect on huntingtin-induced cell death. *J. Cell Biol.* **171**, 603–614 (2005).
13. Kirkin, V. et al. A role for NBR1 in autophagosomal degradation of ubiquitinated substrates. *Mol. Cell* **33**, 505–516 (2009).
14. Sun, D., Wu, R., Zheng, J., Li, P. & Yu, L. Polyubiquitin chain-induced p62 phase separation drives autophagic cargo segregation. *Cell Res.* **28**, 405–415 (2018).
15. Zaffagnini, G. et al. p62 filaments capture and present ubiquitinated cargos for autophagy. *EMBO J.* **37**, e98308 (2018).
16. Turco, E. et al. Reconstitution defines the roles of p62, NBR1, and TAX1BP1 in ubiquitin condensate formation and autophagy initiation. *Nat. Commun.* **12**, 5212 (2021).
17. Ohnstad, A. E. et al. Receptor-mediated clustering of FIP200 bypasses the role of LC3 lipidation in autophagy. *EMBO J.* **39**, e104948 (2020).
18. Sarraf, S. A. et al. Loss of TAX1BP1-directed autophagy results in protein aggregate accumulation in the brain. *Mol. Cell* **80**, 779–795 e710 (2020).
19. Swatek, K. N. & Komander, D. Ubiquitin modifications. *Cell Res.* **26**, 399–422 (2016).
20. Yau, R. & Rape, M. The increasing complexity of the ubiquitin code. *Nat. Cell Biol.* **18**, 579–586 (2016).
21. Oh, E., Akopian, D. & Rape, M. Principles of ubiquitin-dependent signaling. *Annu Rev. Cell Dev. Biol.* **34**, 137–162 (2018).
22. Dikic, I., Schulman, B. A. An expanded lexicon for the ubiquitin code. *Nat. Rev. Mol. Cell Biol.* **24**, 1–15 (2022).
23. Kirisako, T. et al. A ubiquitin ligase complex assembles linear polyubiquitin chains. *EMBO J.* **25**, 4877–4887 (2006).
24. Iwai, K. Discovery of linear ubiquitination, a crucial regulator for immune signaling and cell death. *FEBS J.* **288**, 1060–1069 (2021).
25. Fiil, B. K. & Gyrd-Hansen, M. The Met1-linked ubiquitin machinery in inflammation and infection. *Cell Death Differ.* **28**, 557–569 (2021).
26. Fuseya, Y. & Iwai, K. Biochemistry, pathophysiology, and regulation of linear ubiquitination: intricate regulation by coordinated functions of the associated ligase and deubiquitinase. *Cells* **10**, 2706 (2021).
27. Jahan, A. S., Elbaek, C. R. & Damgaard, R. B. Met1-linked ubiquitin signalling in health and disease: inflammation, immunity, cancer, and beyond. *Cell Death Differ.* **28**, 473–492 (2021).
28. Oikawa, D., Sato, Y., Ito, H. & Tokunaga, F. Linear ubiquitin code: its writer, erasers, decoders, inhibitors, and implications in disorders. *Int J. Mol. Sci.* **21**, 3381 (2020).
29. Dittmar, G. & Winklhofer, K. F. Linear ubiquitin chains: cellular functions and strategies for detection and quantification. *Front. Chem.* **7**, 915 (2019).
30. Rittinger, K. & Ikeda, F. Linear ubiquitin chains: enzymes, mechanisms and biology. *Open Biol.* **7**, 170026 (2017).
31. Hrdinka, M. & Gyrd-Hansen, M. The Met1-linked ubiquitin machinery: emerging themes of (De)regulation. *Mol. Cell* **68**, 265–280 (2017).
32. Tokunaga, F. & Ikeda, F. Linear ubiquitination in immune and neurodegenerative diseases, and beyond. *Biochem. Soc. Trans.* **50**, 799–811 (2022).
33. Shibata, Y. & Komander, D. Lubac. *Curr. Biol.* **32**, R506–R508 (2022).
34. Spit, M., Rieser, E. & Walczak, H. Linear ubiquitination at a glance. *J. Cell Sci.* **132**, jcs208512 (2019).
35. Zinngrebe, J. & Walczak, H. TLRs go linear - on the ubiquitin edge. *Trends Mol. Med.* **23**, 296–309 (2017).
36. Sasaki, K. & Iwai, K. Roles of linear ubiquitinylation, a crucial regulator of NF-kappaB and cell death, in the immune system. *Immunol. Rev.* **266**, 175–189 (2015).
37. Ikeda, F. Linear ubiquitination signals in adaptive immune responses. *Immunol. Rev.* **266**, 222–236 (2015).
38. Iwai, K., Fujita, H. & Sasaki, Y. Linear ubiquitin chains: NF-kappaB signalling, cell death and beyond. *Nat. Rev. Mol. Cell Biol.* **15**, 503–508 (2014).
39. Maubach, G., Schmadicke, A. C. & Naumann, M. NEMO links nuclear factor-kappaB to human diseases. *Trends Mol. Med.* **23**, 1138–1155 (2017).
40. Clark, K., Nanda, S. & Cohen, P. Molecular control of the NEMO family of ubiquitin-binding proteins. *Nat. Rev. Cancer* **13**, 673–685 (2013).
41. Israel, A. The IKK complex, a central regulator of NF-kappaB activation. *Cold Spring Harb. Perspect. Biol.* **2**, a000158 (2010).
42. Annibaldi, A. & Meier, P. Checkpoints in TNF-induced cell death: implications in inflammation and cancer. *Trends Mol. Med.* **24**, 49–65 (2018).
43. Brenner, D., Blaser, H. & Mak, T. W. Regulation of tumour necrosis factor signalling: live or let die. *Nat. Rev. Immunol.* **15**, 362–374 (2015).
44. Smahi, A. et al. Genomic rearrangement in NEMO impairs NF-kappaB activation and is a cause of incontinentia pigmenti. The International Incontinentia Pigmenti (IP) Consortium. *Nature* **405**, 466–472 (2000).
45. Fusco, F. et al. EDA-ID and IP, two faces of the same coin: how the same IKBKG/NEMO mutation affecting the NF-kappaB pathway can cause immunodeficiency and/or inflammation. *Int. Rev. Immunol.* **34**, 445–459 (2015).
46. Conte, M. I. et al. Insight into IKBKG/NEMO locus: report of new mutations and complex genomic rearrangements leading to incontinentia pigmenti disease. *Hum. Mutat.* **35**, 165–177 (2014).
47. Narayanan, M. J., Rangasamy, S. & Narayanan, V. Incontinentia pigmenti (Bloch-Sulzberger syndrome). *Handb. Clin. Neurol.* **132**, 271–280 (2015).
48. Cammarata-Scalisi, F., Fusco, F. & Ursini, M. V. Incontinentia Pigmenti. *Actas Dermosifiliogr.* **110**, 273–278 (2019).
49. van Well, E. M. et al. A protein quality control pathway regulated by linear ubiquitination. *EMBO J.* **38**, e100730 (2019).
50. Goel, S. et al. Linear ubiquitination induces NEMO phase separation to activate NF-kappaB signaling. *Life Sci. Alliance* **6**, e202201607 (2023).
51. Gupta, R. et al. Firefly luciferase mutants as sensors of proteome stress. *Nat. Methods* **8**, 879–884 (2011).
52. Blumenstock, S. et al. Fluc-EGFP reporter mice reveal differential alterations of neuronal proteostasis in aging and disease. *EMBO J.* **40**, e107260 (2021).
53. Polinski, N. K. et al. Best Practices for Generating and Using Alpha-Synuclein Pre-Formed Fibrils to Model Parkinson's Disease in Rodents. *J. Parkinsons Dis.* **8**, 303–322 (2018).
54. Volpicelli-Daley, L. A., Luk, K. C. & Lee, V. M. Addition of exogenous alpha-synuclein preformed fibrils to primary neuronal cultures to seed recruitment of endogenous alpha-synuclein to Lewy body and Lewy neurite-like aggregates. *Nat. Protoc.* **9**, 2135–2146 (2014).
55. Trinkaus, V. A. et al. In situ architecture of neuronal alpha-Synuclein inclusions. *Nat. Commun.* **12**, 2110 (2021).

56. Matsumoto, M. L. et al. Engineering and structural characterization of a linear polyubiquitin-specific antibody. *J. Mol. Biol.* **418**, 134–144 (2012).
57. Tokunaga, F. et al. Involvement of linear polyubiquitylation of NEMO in NF-kappaB activation. *Nat. Cell Biol.* **11**, 123–132 (2009).
58. Fujita, H. et al. Mechanism underlying I kappa B kinase activation mediated by the linear ubiquitin chain assembly complex. *Mol. Cell Biol.* **34**, 1322–1335 (2014).
59. Rahighi, S., Iyer, M., Oveisi, H., Nasser, S. & Duong, V. Structural basis for the simultaneous recognition of NEMO and acceptor ubiquitin by the HOIP NZF1 domain. *Sci. Rep.* **12**, 12241 (2022).
60. Hubeau, M. et al. New mechanism of X-linked anhidrotic ectodermal dysplasia with immunodeficiency: impairment of ubiquitin binding despite normal folding of NEMO protein. *Blood* **118**, 926–935 (2011).
61. Rahighi, S. et al. Specific recognition of linear ubiquitin chains by NEMO is important for NF-kappaB activation. *Cell* **136**, 1098–1109 (2009).
62. Noad, J., von der Malsburg, A., Pathe, C., Michel, M. A., Komander, D. & Randow, F. LUBAC-synthesized linear ubiquitin chains restrict cytosol-invading bacteria by activating autophagy and NF-kappaB. *Nat. Microbiol.* **2**, 17063 (2017).
63. van Wijk, S. J. L. et al. Linear ubiquitination of cytosolic Salmonella Typhimurium activates NF-kappaB and restricts bacterial proliferation. *Nat. Microbiol.* **2**, 17066 (2017).
64. Otten, E. G. et al. Ubiquitylation of lipopolysaccharide by RNF213 during bacterial infection. *Nature* **594**, 111–116 (2021).
65. Stefanis, L., Emmanouilidou, E., Pantazopoulou, M., Kirik, D., Vekrellis, K. & Tofaris, G. K. How is alpha-synuclein cleared from the cell? *J. Neurochem.* **150**, 577–590 (2019).
66. Sahoo, S., Padhy, A. A., Kumari, V. & Mishra, P. Role of ubiquitin-proteasome and autophagy-lysosome pathways in alpha-synuclein aggregate clearance. *Mol. Neurobiol.* **59**, 5379–5407 (2022).
67. Lashuel, H. A., Overk, C. R., Oueslati, A. & Masliah, E. The many faces of alpha-synuclein: from structure and toxicity to therapeutic target. *Nat. Rev. Neurosci.* **14**, 38–48 (2013).
68. Lamark, T., Svenning, S. & Johansen, T. Regulation of selective autophagy: the p62/SQSTM1 paradigm. *Essays Biochem.* **61**, 609–624 (2017).
69. Pankiv, S. et al. p62/SQSTM1 binds directly to Atg8/LC3 to facilitate degradation of ubiquitinated protein aggregates by autophagy. *J. Biol. Chem.* **282**, 24131–24145 (2007).
70. Danieli, A. & Martens, S. p62-mediated phase separation at the intersection of the ubiquitin-proteasome system and autophagy. *J. Cell Sci.* **131**, jcs214304 (2018).
71. Wurzer, B. et al. Oligomerization of p62 allows for selection of ubiquitinated cargo and isolation membrane during selective autophagy. *eLife* **4**, e08941 (2015).
72. Zotti, T. et al. TRAF6-mediated ubiquitination of NEMO requires p62/sequestosome-1. *Mol. Immunol.* **58**, 27–31 (2014).
73. Martin, P., Diaz-Meco, M. T. & Moscat, J. The signaling adapter p62 is an important mediator of T helper 2 cell function and allergic airway inflammation. *EMBO J.* **25**, 3524–3533 (2006).
74. Harding, O., Holzer, E., Riley, J. F., Martens, S. & Holzbaur, E. L. F. Damaged mitochondria recruit the effector NEMO to activate NF-kappaB signaling. *Mol. Cell* **83**, 3188–3204 e3187 (2023).
75. Kuusisto, E., Salminen, A. & Alafuzoff, I. Ubiquitin-binding protein p62 is present in neuronal and glial inclusions in human tauopathies and synucleinopathies. *Neuroreport* **12**, 2085–2090 (2001).
76. Trejo-Lopez, J. A. et al. Generation and characterization of novel monoclonal antibodies targeting p62/sequestosome-1 across human neurodegenerative diseases. *J. Neuropathol. Exp. Neurol.* **79**, 407–418 (2020).
77. Turco, E. et al. FIP200 claw domain binding to p62 promotes autophagosome formation at ubiquitin condensates. *Mol. Cell* **74**, 330–346 e311 (2019).
78. Jakobi, A. J. et al. Structural basis of p62/SQSTM1 helical filaments and their role in cellular cargo uptake. *Nat. Commun.* **11**, 440 (2020).
79. Du, M., Ea, C. K., Fang, Y. & Chen, Z. J. Liquid phase separation of NEMO induced by polyubiquitin chains activates NF-kappaB. *Mol. Cell* **82**, 2415–2426.e5 (2022).
80. Emmerich, C. H. et al. Activation of the canonical IKK complex by K63/M1-linked hybrid ubiquitin chains. *Proc. Natl Acad. Sci. USA* **110**, 15247–15252 (2013).
81. Yamasaki, A. et al. Liquidity Is a Critical Determinant for Selective Autophagy of Protein Condensates. *Mol. Cell* **77**, 1163–1175 e1169 (2020).
82. Gallagher, E. R. & Holzbaur, E. L. F. The selective autophagy adaptor p62/SQSTM1 forms phase condensates regulated by HSP27 that facilitate the clearance of damaged lysosomes via lysophagy. *Cell Rep.* **42**, 112037 (2023).
83. Ma, X., Zhang, M. & Ge, L. A switch of chaperonin function regulates the clearance of solid protein aggregates. *Autophagy* **18**, 2746–2748 (2022).
84. Peng, S. Z. et al. Phase separation of Nur77 mediates celastrol-induced mitophagy by promoting the liquidity of p62/SQSTM1 condensates. *Nat. Commun.* **12**, 5989 (2021).
85. Kageyama, S. et al. p62/SQSTM1-droplet serves as a platform for autophagosome formation and anti-oxidative stress response. *Nat. Commun.* **12**, 16 (2021).
86. Komander, D., Reyes-Turcu, F., Licchesi, J. D., Odenwaelder, P., Wilkinson, K. D. & Barford, D. Molecular discrimination of structurally equivalent Lys 63-linked and linear polyubiquitin chains. *EMBO Rep.* **10**, 466–473 (2009).
87. Wagner, S. et al. Ubiquitin binding mediates the NF-kappaB inhibitory potential of ABIN proteins. *Oncogene* **27**, 3739–3745 (2008).
88. Lo, Y. C. et al. Structural basis for recognition of diubiquitins by NEMO. *Mol. Cell* **33**, 602–615 (2009).
89. Laplantine, E. et al. NEMO specifically recognizes K63-linked polyubiquitin chains through a new bipartite ubiquitin-binding domain. *EMBO J.* **28**, 2885–2895 (2009).
90. Cordier, F., Grubisha, O., Traincard, F., Veron, M., Delepiepierre, M. & Agou, F. The zinc finger of NEMO is a functional ubiquitin-binding domain. *J. Biol. Chem.* **284**, 2902–2907 (2009).
91. Schrofelbauer, B., Polley, S., Behar, M., Ghosh, G. & Hoffmann, A. NEMO ensures signaling specificity of the pleiotropic IKKbeta by directing its kinase activity toward I kappa Balpha. *Mol. Cell* **47**, 111–121 (2012).
92. Zilberman-Rudenko, J. et al. Recruitment of A20 by the C-terminal domain of NEMO suppresses NF-kappaB activation and autoinflammatory disease. *Proc. Natl Acad. Sci. USA* **113**, 1612–1617 (2016).
93. Herhaus, L. et al. Molecular recognition of M1-linked ubiquitin chains by native and phosphorylated UBAN domains. *J. Mol. Biol.* **431**, 3146–3156 (2019).
94. Merline, R. et al. A20 binding and inhibitor of nuclear factor kappa B (NF-kappaB)-1 (ABIN-1): a novel modulator of mitochondrial autophagy. *Am. J. Physiol. Cell Physiol.* **324**, C339–C352 (2023).
95. Tusco, R. et al. Kenny mediates selective autophagic degradation of the IKK complex to control innate immune responses. *Nat. Commun.* **8**, 1264 (2017).
96. Wu, Z. et al. LUBAC assembles a ubiquitin signaling platform at mitochondria for signal amplification and transport of NF-kappaB to the nucleus. *EMBO J.* **41**, e112006 (2022).
97. Jain, A. et al. p62/SQSTM1 is a target gene for transcription factor NRF2 and creates a positive feedback loop by inducing

- antioxidant response element-driven gene transcription. *J. Biol. Chem.* **285**, 22576–22591 (2010).
98. Meffert, M. K., Chang, J. M., Wiltgen, B. J., Fanselow, M. S., Baltimore, D. & NF-kappa B. functions in synaptic signaling and behavior. *Nat. Neurosci.* **6**, 1072–1078 (2003).
  99. Neidl, R. et al. Late-life environmental enrichment induces acetylation events and nuclear factor kappaB-dependent regulations in the hippocampus of aged rats showing improved plasticity and learning. *J. Neurosci.* **36**, 4351–4361 (2016).
  100. O’Riordan, K. J. et al. Regulation of nuclear factor kappaB in the hippocampus by group I metabotropic glutamate receptors. *J. Neurosci.* **26**, 4870–4879 (2006).
  101. Dresselhaus, E. C., Boersma, M. C. H. & Meffert, M. K. Targeting of NF-kappaB to dendritic spines is required for synaptic signaling and spine development. *J. Neurosci.* **38**, 4093–4103 (2018).
  102. Bhakar, A. L. et al. Constitutive nuclear factor-kappa B activity is required for central neuron survival. *J. Neurosci.* **22**, 8466–8475 (2002).
  103. Blondeau, N., Widmann, C., Lazdunski, M. & Heurteaux, C. Activation of the nuclear factor-kappaB is a key event in brain tolerance. *J. Neurosci.* **21**, 4668–4677 (2001).
  104. Cheng, B., Christakos, S. & Mattson, M. P. Tumor necrosis factors protect neurons against metabolic-excitotoxic insults and promote maintenance of calcium homeostasis. *Neuron* **12**, 139–153 (1994).
  105. Turrin, N. P. & Rivest, S. Tumor necrosis factor alpha but not interleukin 1 beta mediates neuroprotection in response to acute nitric oxide excitotoxicity. *J. Neurosci.* **26**, 143–151 (2006).
  106. Carter, B. D. et al. Selective activation of NF-kappa B by nerve growth factor through the neurotrophin receptor p75. *Science* **272**, 542–545 (1996).
  107. Foehr, E. D., Lin, X., O’Mahony, A., Gelezianas, R., Bradshaw, R. A., Greene, W. C. & NF-kappa B. signaling promotes both cell survival and neurite process formation in nerve growth factor-stimulated PC12 cells. *J. Neurosci.* **20**, 7556–7563 (2000).
  108. Nakajima, K. et al. Neurotrophins regulate the function of cultured microglia. *Glia* **24**, 272–289 (1998).
  109. Hayashi, H. et al. Characterization of intracellular signals via tyrosine 1062 in RET activated by glial cell line-derived neurotrophic factor. *Oncogene* **19**, 4469–4475 (2000).
  110. Meka, D. P. et al. Parkin cooperates with GDNF/RET signaling to prevent dopaminergic neuron degeneration. *J. Clin. Invest.* **125**, 1873–1885 (2015).
  111. Muller-Rischart, A. K. et al. The E3 ligase parkin maintains mitochondrial integrity by increasing linear ubiquitination of NEMO. *Mol. Cell* **49**, 908–921 (2013).
  112. Henn, I. H. et al. Parkin mediates neuroprotection through activation of IkkappaB kinase/nuclear factor-kappaB signaling. *J. Neurosci.* **27**, 1868–1878 (2007).
  113. Ayaki, T. et al. Multiple proteinopathies in familial ALS cases with optineurin mutations. *J. Neuropathol. Exp. Neurol.* **77**, 128–138 (2018).
  114. Richards, S. et al. Standards and guidelines for the interpretation of sequence variants: a joint consensus recommendation of the American College of Medical Genetics and Genomics and the Association for Molecular Pathology. *Genet. Med.* **17**, 405–424 (2015).
  115. Schmidt-Supprian, M. et al. NEMO/IKK gamma-deficient mice model incontinentia pigmenti. *Mol. Cell* **5**, 981–992 (2000).
  116. Komatsu, M. et al. Homeostatic levels of p62 control cytoplasmic inclusion body formation in autophagy-deficient mice. *Cell* **131**, 1149–1163 (2007).

## Acknowledgements

We thank Tetsuro Ishii for p62 KO MEFs, Marc Schmidt-Supprian for NEMO KO MEFs, Terje Johansen for p62 plasmids, Sascha Martens for mCherry-p62, Yen-Ting Chen for discussing protein adsorption processes, and Genentech for the 1F11/3F5/Y102L antibody. We also thank Bruce Conklin (Gladstone Institutes) and the Gladstone Stem Cell Core for assistance with the patient skin biopsy and fibroblast culture. This work was supported by the German Research Foundation (WI/2111-4, WI/2111-6, WI/2111-8, FOR 2848 to KFW) and Germany’s Excellence Strategy EXC 2033 390677874 – RESOLV (to KFW and JT) and EXC 2145 390857198 – SyNergy (to CB and FUH), the NIH (R01 AG065428 to KN) as well as by the joint efforts of The Michael J. Fox Foundation for Parkinson’s Research (MJFF) and the Aligning Science Across Parkinson’s (ASAP) initiative. MJFF administers the grant ASAP-000282 on behalf of ASAP and itself. SR-SIM microscopy was funded by the German Research Foundation and the State Government of North Rhine-Westphalia (INST 213/840-1 FUGG).

## Author contributions

Conceptualization: N.F., L.A., V.B., S.G., A.S.-V., C.Sachse., C.B., K.N., C.W.C., J.T. and K.F.W. Validation: N.F., L.A., V.B., A.B., S.G., A.S.-V., L.J.K., S.A.C., P.G., V.A.T., E.M.v.W., M.J., A.W., L.J., J.T. and K.F.W. Visualization: N.F., L.A., V.B., A.B., S.G., A.S.-V., V.A.T., M.J., E.J.H., J.T. and K.F.W. Writing—original draft: N.F., V.B., A.B., S.G., A.S.-V., J.T. and K.F.W. Writing – review & editing: L.J.K., S.A.C., K.T., R.B.D., A.W., C.K., C.B., M.G., F.U.H., K.N., C.W.C. and E.J.H. Formal analysis: N.F., L.A., V.B., A.B., S.G., A.S.-V., L.J.K., S.A.C., P.G., E.M.v.W., M.J., A.W. and L.J. Methodology: N.F., L.A., V.B., A.B., S.G., A.S.-V., V.A.T., M.J., A.W., C.K., L.J. and E.J.H. Investigation: N.F., L.A., V.B., A.B., S.G., A.S.-V., L.J.K., S.A.C., P.G., V.A.T., E.M.v.W., M.J., A.W., C.K., L.J. and E.J.H. Data curation: N.F., L.A., V.B. and S.G. Resources: L.J.K., S.A.C., K.T., R.B.D., C.Sachse, G.E., A.K., B.E., C.Saft, C.B., M.G., F.U.H., K.N., C.W.C., E.J.H., R.G. Supervision: J.T. and K.F.W. Funding acquisition: K.F.W. Project administration: J.T. and K.F.W.

## Funding

Open Access funding enabled and organized by Projekt DEAL.

## Competing interests

R.B.D. is a scientific advisor for Immagine B.V. C.K. serves as a medical advisor to Centogene for the validation of genetic testing reports in the field of movement disorders and dementia, excluding Parkinson’s disease, and Retromer Therapeutics and received speakers’ honoraria from Bial and Desitin. The remaining authors declare no competing interests.

## Additional information

**Supplementary information** The online version contains supplementary material available at <https://doi.org/10.1038/s41467-023-44033-0>.

**Correspondence** and requests for materials should be addressed to Konstanze F. Winklhofer.

**Peer review information** *Nature Communications* thanks Eun-Jin Bae, Ivan Dikic, and the other, anonymous, reviewer(s) for their contribution to the peer review of this work. A peer review file is available.

**Reprints and permissions information** is available at <http://www.nature.com/reprints>

**Publisher’s note** Springer Nature remains neutral with regard to jurisdictional claims in published maps and institutional affiliations.



**Open Access** This article is licensed under a Creative Commons Attribution 4.0 International License, which permits use, sharing, adaptation, distribution and reproduction in any medium or format, as long as you give appropriate credit to the original author(s) and the source, provide a link to the Creative Commons licence, and indicate if changes were made. The images or other third party material in this article are included in the article's Creative Commons licence, unless indicated otherwise in a credit line to the material. If material is not included in the article's Creative Commons licence and your intended use is not permitted by statutory regulation or exceeds the permitted use, you will need to obtain permission directly from the copyright holder. To view a copy of this licence, visit <http://creativecommons.org/licenses/by/4.0/>.

© The Author(s) 2023

---

<sup>1</sup>Department Molecular Cell Biology, Institute of Biochemistry and Pathobiochemistry, Ruhr University Bochum, 44801 Bochum, Germany. <sup>2</sup>Department Biochemistry of Neurodegenerative Diseases, Institute of Biochemistry and Pathobiochemistry, Ruhr University Bochum, 44801 Bochum, Germany. <sup>3</sup>Department of Neurology, St Josef Hospital, Ruhr University Bochum, 44791 Bochum, Germany. <sup>4</sup>Cluster of Excellence RESOLV, 44801 Bochum, Germany. <sup>5</sup>Department of Cellular Biochemistry, Max Planck Institute of Biochemistry, 82152 Martinsried, Germany. <sup>6</sup>Analytical Chemistry II, Faculty of Chemistry and Biochemistry, Ruhr University Bochum, 44801 Bochum, Germany. <sup>7</sup>Department of Biotechnology and Biomedicine, Technical University of Denmark, 2800 Kongens Lyngby, Denmark. <sup>8</sup>Charité - Universitätsmedizin Berlin, Corporate Member of Freie Universität Berlin and Humboldt-Universität zu Berlin, Department of Neuropathology, Charitéplatz 1, 10117 Berlin, Germany. <sup>9</sup>Institute of Neurogenetics, University of Lübeck, Lübeck, Germany. <sup>10</sup>Ernst-Ruska Centre for Microscopy and Spectroscopy with Electrons (ER-C-3/Structural Biology), Forschungszentrum Jülich, Jülich, Germany. <sup>11</sup>Institute for Biological Information Processing (IBI-6/Cellular Structural Biology), Forschungszentrum Jülich, Jülich, Germany. <sup>12</sup>Department of Biology, Heinrich Heine University, Düsseldorf, Germany. <sup>13</sup>Munich Cluster for Systems Neurology, Faculty of Medicine, Ludwig-Maximilians-Universität München, Munich, Germany. <sup>14</sup>Institute of Neuropathology, University Medical Center Hamburg-Eppendorf, Martinistraße 52, 20251 Hamburg, Germany. <sup>15</sup>Munich Cluster for Systems Neurology (SyNergy), 81377 Munich, Germany. <sup>16</sup>Gladstone Institute of Neurological Disease, Gladstone Institutes, San Francisco, CA, USA. <sup>17</sup>Department of Neurology, University of California, San Francisco, CA, USA. <sup>18</sup>Weill Institute for Neurosciences, University of California San Francisco, San Francisco, CA, USA. <sup>19</sup>Department of Pathology, University of California, San Francisco, CA, USA. <sup>20</sup>Present address: Department of Neurology, Klinikum Dortmund, University Witten/Herdecke, 44135 Dortmund, Germany. <sup>21</sup>Present address: Center for Neuropathology and Prion Research, Ludwig-Maximilians University, 81377 Munich, Germany. ✉e-mail: [konstanze.winklhofer@rub.de](mailto:konstanze.winklhofer@rub.de)